

Boiling flow estimation for aero-optic phase screen generation

Jeffrey W. Utley^{a,*}, Gregery T. Buzzard^a, Charles A. Bouman^b, Matthew R. Kemnetz^c

^aPurdue University, Department of Mathematics, West Lafayette, Indiana 47907, USA

^bPurdue University, Departments of Electrical and Computer Engineering and Biomedical Engineering, West Lafayette, Indiana 47907, USA

^cAir Force Institute of Technology, Department of Engineering Physics, Wright-Patterson AFB, OH 45433, USA

Abstract. Aero-optic effects due to turbulence can reduce the effectiveness of transmitting light waves to a distant target. Methods to compensate for turbulence typically rely on realistic turbulence data, which can be generated by i) experiment, ii) high-fidelity CFD, iii) low-fidelity CFD, and iv) autoregressive methods. However, each of these methods has significant drawbacks, including monetary and/or computational expense, limited quantity, inaccurate statistics, and overall complexity. In contrast, the boiling flow algorithm is a simple, computationally efficient model that can generate atmospheric phase screen data with only a handful of parameters. However, boiling flow has not been widely used in aero-optic applications, at least in part because some of these parameters, such as r_0 , are not clearly defined for aero-optic data. In this paper, we demonstrate a method to use the boiling flow algorithm to generate arbitrary length synthetic data to match the statistics of measured aero-optic data. Importantly, we modify the standard boiling flow method to generate anisotropic phase screens. While this model does not fully capture all statistics, it can be used to generate data that matches the temporal power spectrum or the anisotropic 2D structure function, with the ability to trade fidelity to one for fidelity to the other.

Keywords: Aero-optics, turbulent boundary layer, phase screens, wavefront aberrations, frozen flow, boiling flow.

*Jeffrey W. Utley, utleyj@purdue.edu

1 Introduction

Atmospheric and aerodynamic turbulence distort light wave propagation, thereby reducing the effectiveness of transmitting light waves to a distant target. In particular, both phenomena cause refractive index variations^{1–3} which lead to random phase aberrations.^{4–6} Here, we focus on the phase aberrations induced by aerodynamic turbulence, which are called aero-optic phase aberrations. These spatially and temporally varying phase aberrations can be measured by optical sensors,^{7–9} resulting in a time series of images called aero-optic phase screens. Modern methods to mitigate these aberrations include algorithms such as dynamic mode decomposition,^{10–13} machine learning,^{14–16} and autoregressive modeling.¹⁷ However, each of these methods requires long time series of aero-optic phase screen data to yield adequate training without overfitting in these algorithms.

Measuring long sequences of aero-optic phase screens through experiment is expensive and time intensive,¹⁸ so a variety of simulation methods have been proposed as a less expensive alternative. Computational Fluid Dynamics (CFD) can simulate an aerodynamic flow field,^{2,4,19} from which one can derive the resulting phase aberrations.²⁰⁻²² High-fidelity CFD can accurately model the aerodynamic flow field around well-understood geometries^{4,20,21} but is very computationally expensive,^{2,23,24} while low-fidelity CFD simplifies the complex calculations involved, but gives less accurate results.^{2,23} In contrast, the autoregressive methods introduced by Vogel et al.,²⁵ Utley et al.,²⁶ and Faghihi et al.²⁷ are less computationally expensive and match the statistics of measured aero-optic data. However, these methods use complex statistical models with many unknown parameters.

Although not used previously for generating aero-optic phase screens, the simulation algorithm called boiling flow²⁸ is a computationally efficient algorithm for generating physically-relevant atmospheric phase screens using only five parameters. Introduced in Srinath et al.,²⁸ boiling flow generalizes a simulation method using the Kolmogorov theory of turbulence^{1,28,29} and the Taylor frozen-flow hypothesis.^{25,28-31} Boiling flow has become a common and well-known method for generating atmospheric phase screens.³²⁻⁴⁴ However, boiling flow depends on physical parameters that follow from the Kolmogorov theory of turbulence and the Taylor frozen-flow hypothesis. Moreover, boiling flow produces data with spatially isotropic correlations. Since aero-optic effects do not follow the Kolmogorov theory of turbulence^{25,45} and are spatially anisotropic, this approach has not been used for aero-optic phase screen generation.

In this paper, we introduce a method to use the boiling flow algorithm to generate arbitrary length, spatially anisotropic synthetic data to match the statistics of measured aero-optic data. Our key contributions are as follows:

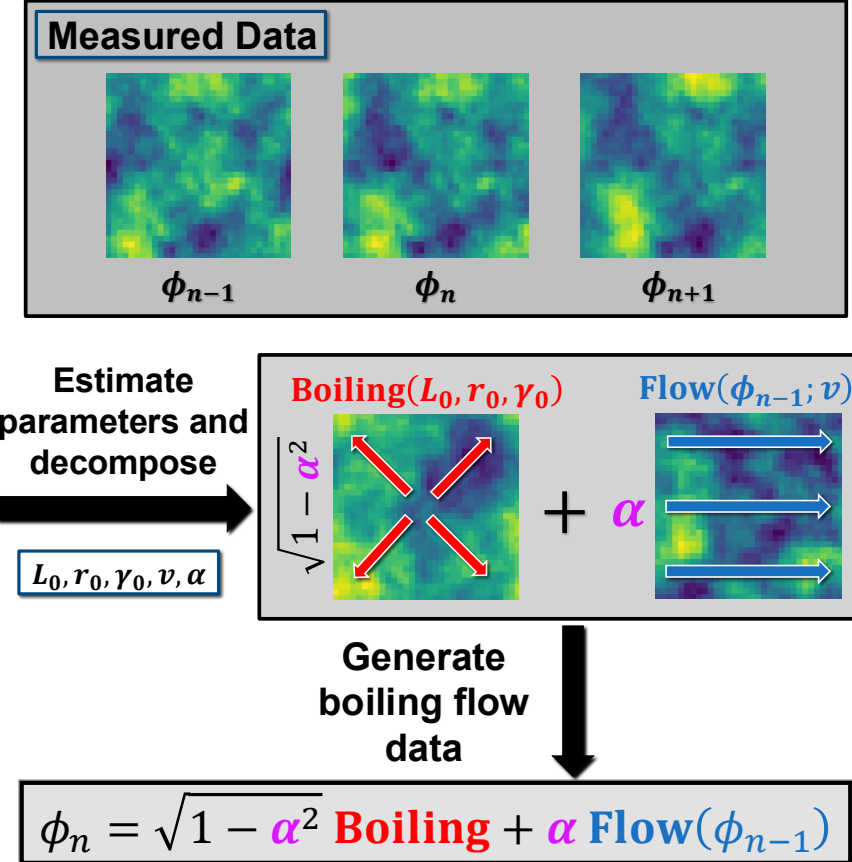


Fig 1: Outline of the boiling flow algorithm as used in this paper. Starting with a time series of measured phase screens ϕ_n , our method estimates the boiling flow parameters and decomposes the data into the weighted sum of a boiling component and a flow component. The method then uses these components and the parameters to generate synthetic phase screens using boiling flow. We introduce the parameter γ_0 into the boiling model to produce spatially anisotropic correlations.

- Instead of interpreting boiling flow parameters as physical quantities, we introduce an algorithm that estimates these parameters to fit the temporal power spectrum of measured data.
- We introduce a new parameter γ_0 to the boiling model to produce spatially anisotropic synthetic data, which can be used to match the 2D structure function of measured data.

Our results show that this method matches the temporal power spectrum (TPS) of measured aero-optic data within 12% when using the standard, isotropic form of boiling and provides a good qualitative fit to the 2D structure function when using the new, anisotropic version.

This paper builds on previous work from Ref. 46. This paper uses the GitHub repository “Boiling Flow,” linked in Ref. 47.

2 Overview of Boiling Flow

Figure 1 shows an outline of boiling flow as used in this paper. Boiling flow depends on physical parameters that follow from the Kolmogorov theory of turbulence and the Taylor frozen-flow hypothesis. These parameters include the wind velocity components (v_x, v_y) , outer scale L_0 , Fried coherence length r_0 , and a flow-coefficient α . Furthermore, here we introduce an anisotropy parameter γ_0 to adjust the spatial correlation length scale for the y -axis separately from the x -axis.

The key idea of boiling flow, as described in greater detail in Ref. 28, is to represent a sequence of phase screens in terms of two distinct components: boiling and flow.

Boiling is a random process with a specified power spectrum associated with Kolmogorov turbulence. In practice, a boiling phase screen is generated in Fourier space following Ref. 29. First define $\Delta_f = 1/(N\Delta)$, where N is the number of pixels along a side in a square phase screen and Δ is the spatial grid spacing in meters per pixel. Then in Fourier space,

$$\tilde{B}_n = \Delta_f \sqrt{V_\phi(\mathbf{k}\Delta_f)} \odot \epsilon_n \quad (\text{Boiling at step } n) \quad (1)$$

Here, \mathbf{k} is an array of 2-component entries, with each component taking integer values from $-N/2$ to $N/2 - 1$. Also, ϵ_n is a 2D-array of complex-valued white noise with variance 1 in each component, and V_ϕ is the idealized Von Kármán spatial power spectral density (PSD) defined in Eq. (5), with input in cycles per meter. \tilde{B}_n depends on L_0 , γ_0 , and r_0 , which determine the PSD through V_ϕ . Also, \odot represents element-wise multiplication.

In contrast, flow is a purely convective term that translates a given phase screen according to the velocity vector $\mathbf{v} = (v_x, v_y)$. Taking $\tilde{\phi}_{n-1}$ to be a phase screen in Fourier space at time-step $n-1$, this gives a translated screen at time-step n

$$\tilde{F}_n = e^{-j(\mathbf{v} \cdot 2\pi\mathbf{k}/N)} \odot \tilde{\phi}_{n-1}. \quad (\text{Flow from } n-1 \text{ to } n) \quad (2)$$

We use F instead of ϕ to indicate that this is the flow component only; this will be combined with the boiling component in Eq. (3). Since the flow is represented in Fourier space, the translation is accomplished by multiplication. \tilde{F}_n depends on the flow velocity \mathbf{v} .

Boiling flow uses an energy-preserving linear combination of these individual terms to model a convective motion that evolves at each step to include the effects of boiling. This yields the Fourier space representation of the phase screen at time step n as

$$\tilde{\phi}_n = \sqrt{1 - \alpha^2} \tilde{B}_n + \alpha \tilde{F}_n. \quad (\text{Boiling Flow}) \quad (3)$$

The scaling by α and $\sqrt{1 - \alpha^2}$ in Eq. (3) ensures that the spatial PSD of each phase screen $\phi_n \in \mathbb{R}^{N \times N}$ is the idealized PSD V_ϕ .

Our generation algorithm starts with a random phase screen $\tilde{\phi}_0 = \tilde{B}_0$ and applies Eq. (3) recursively, with the following modifications:

- First, to reduce the effect of periodicity arising from a circular Fast Fourier Transform (FFT), we generate phase screens of size $4N \times 4N$ and then extract the first $N \times N$ indices from each over-sized screen.
- Second, we remove tilt, tip, and piston (TTP) from each (restricted) phase screen $\phi_n \in \mathbb{R}^{N \times N}$.

$\mathbb{R}^{N \times N}$. This is a common practice for post-processing measured phase screen data,^{7,48,49} so this step improves the physical relevance of the synthetic phase screens.

This method provides a way to generate arbitrary-duration time series of physically-relevant phase screens.

3 Boiling Flow Parameter Estimation

Section 2 showed that the primary parameters of boiling flow are L_0 , γ_0 , and r_0 to describe boiling, v_x and v_y to determine the flow velocity, and α to determine the ratio of the boiling term to the flow term. Many applications of boiling flow select these parameters based on a desired physical environment,^{32,33,36–38,41,42} where L_0 , r_0 , and the magnitude of (v_x, v_y) are derived from a combination of the Kolmogorov theory of turbulence^{29,50,51} and the Taylor frozen-flow hypothesis.^{38,52} However, because aero-optic effects do not follow the Kolmogorov theory of turbulence,^{25,45} we need to develop and justify an approach to estimate these parameters from measured aero-optic phase screen data.

Existing algorithms designed for atmospheric turbulence could be used to estimate (L_0, r_0) from measured phase aberration data. For example, Refs. 53–55 and Ref. 56 estimate L_0 and r_0 (respectively) from the spatial covariance of the angle-of-arrival (AA) measurements. However, these models are designed for data with non-zero tip/tilt terms, whereas tip/tilt are generally removed from measured aero-optic phase screen data.^{7,48,49} In contrast, Ref. 57 presents two methods to estimate (L_0, r_0) from tip/tilt-corrected phase screen data: (1) fitting the structure function and (2) fitting the Zernike modes of AA measurements. However, the former approach uses a grid-search algorithm for chosen values of L_0 and the latter method involves complex calculations (e.g., matrix inversion, singular value decomposition) to take Zernike modes with a non-circular

aperture. Similarly, Ref. 58 estimates (L_0, r_0) from the Zernike modes of phase screens, but uses an iterative algorithm with multiple least-squares calculations to solve an optimization problem which is not shown be convex.

One existing method for estimating the velocity components (v_x, v_y) is Poyneer et al.,³¹ which uses a heuristic grid search over velocity vectors. An extension of this method to estimate α using the width of the temporal power spectrum (TPS) peak(s) is found in Refs. 28, 35. However, the basic method is designed for frozen flow with multiple wind layers rather than the single layer setting considered here.

In this section, we estimate the boiling flow parameters from a training data set containing a time series of $M \times N$ images. We note that Eq. (3) is not linear in these parameters, so it is difficult to construct a convex loss function that depends on all parameters. Instead, we estimate each parameter with appropriate methods.

- We set L_0 to the width (in meters) of the aperture.
- For the isotropic boiling model, we use per-frequency scaling by $(r_0(\mathbf{f}))^{-5/3}$ to match the unit-scale Von Kárman PSD²⁹ to the spatial PSD of the measured data, then average over frequency to estimate the value of r_0 (in meters).
- For the anisotropic boiling model, we fix a value of γ_0 (unitless), then estimate $r_0 = r_0(\gamma_0)$ as above. Then we choose γ_0 to minimize the mean-squared error between the 2D structure function of the resulting boiling and the 2D structure function of the data.
- We find the flow velocity \mathbf{v} (in pixels per time-step) that maximizes the spatial cross-correlation between TTP-removed frames at multiple time lags, while accounting for the uncertainty induced by boiling.

- We find the flow-coefficient α (unitless) by minimizing the mean-squared error in Fourier space between the measured $\tilde{\phi}_n$ and the predicted flow $\alpha\tilde{F}_n$, obtained as in Eq. (2) by flowing one time step starting from $\tilde{\phi}_{n-1}$.

A key challenge in the estimation of v is the tension between using a longer time lag to better estimate the flow and the confounding effect of boiling, which decreases the correlation between screens separated by long time lags. We describe this challenge and details of each estimation procedure in further detail below.

3.1 Estimating the Boiling Parameters

Estimation of the boiling parameters L_0 and r_0 begins with understanding their role in the boiling model. The outer scale L_0 is defined as the upper bound of the size of turbulent eddies in the atmosphere.²⁹ However, the effect of turbulent eddies larger than the aperture is minimal in tip/tilt/piston (TTP)-removed phase screen data, which is common for aero-optic data.^{7,48,49} Also, in the case of isotropic turbulence, the Fried coherence length r_0 is defined as the diameter over which the mean-squared phase error is at most one radian.^{29,51} However, aero-optic phase aberrations are typically anisotropic,^{25,45} and r_0 alone does not capture this anisotropy. Thus, both parameters require adaptation to measured TTP-removed aero-optic data.

Figure 2, left, illustrates our algorithm for estimating the boiling parameters (L_0, r_0) to fit an isotropic model to the spatial PSD of the training data. Figure 2, right, describes our interpretation of the Fried coherence length r_0 in terms of the spatial PSD.

To estimate L_0 , we note first that because turbulent eddies larger than the aperture mostly result in tip/tilt aberrations instead of higher-order phase aberrations,² removing tip/tilt from phase screen data significantly reduces the effects on large eddies. Further, Siegenthaler et al.⁴⁹ show that

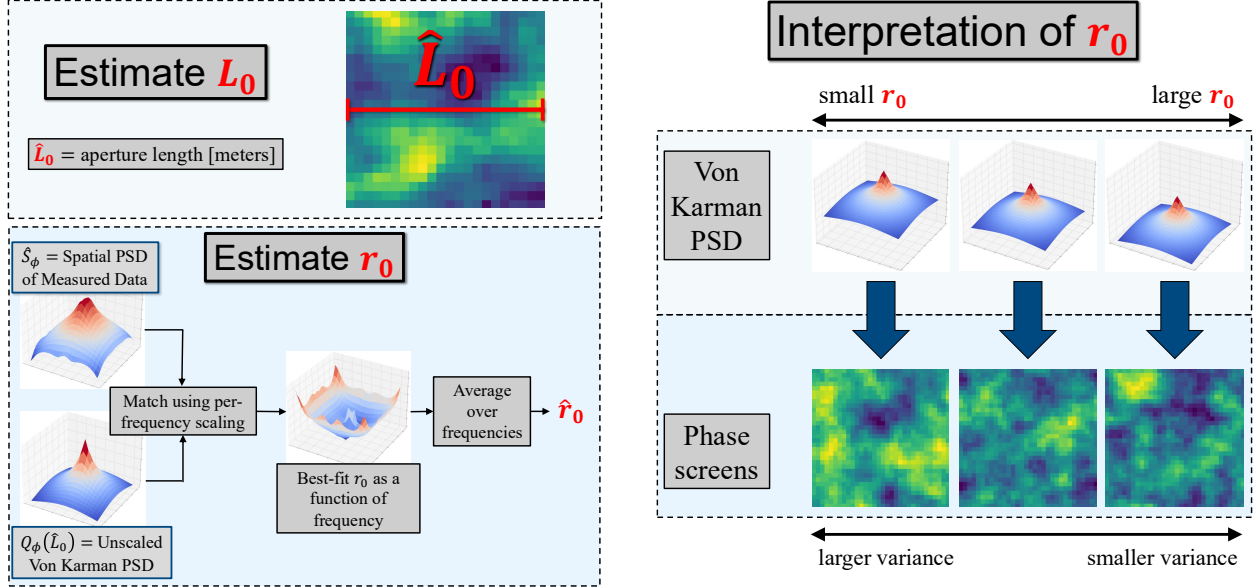


Fig 2: Left: Estimation of the boiling parameters (L_0, r_0) . We set \hat{L}_0 to the aperture length in meters. We then do per-frequency scaling by $(r_0(f))^{-5/3}$ of the unit-scale Von Kármán PSD to match the spatial PSD of the measured data. Then we average over frequencies to obtain \hat{r}_0 . **Right:** Instead of regarding r_0 as a length scale, we interpret it as a scaling parameter for the spatial PSD of phase screens. Smaller r_0 corresponds to larger variance of the phase screens.

tip/tilt removal restricts the (temporal) period of phase aberration data to be at most the aperture size; under the frozen-flow hypothesis, this period is proportional to the size of turbulent eddies.²⁹ Thus, we set \hat{L}_0 to the length of the aperture of the measured data, which is the upper bound of the size of turbulent eddies that have a meaningful effect on the measured phase screen data.

To estimate r_0 in a way that generalizes to the anisotropic case, we consider the effect of r_0 on the Von Kármán PSD, which is commonly used to generate spatially isotropic random phase screens.²⁹ As described more precisely below and illustrated in Fig. 2, we first do a frequency dependent scaling of the Von Kármán PSD to match the spatial PSD of the measured data, then average over frequency to estimate r_0 .

To extend this to the anisotropic case, we introduce a unitless parameter γ_0 to modulate the correlation length scale in the vertical direction independently from the horizontal direction. More

precisely, we incorporate γ_0 through the function Q_ϕ , defined as

$$Q_\phi(\mathbf{f}; \gamma_0) = \frac{0.023}{(f_x^2 + \gamma_0 f_y^2 + L_0^{-2})^{\frac{11}{6}}}. \quad (4)$$

Here, $\mathbf{f} \in \mathbb{R}^2$ is the frequency vector (in cycles per meter) with components (f_x, f_y) in the x - and y -directions, respectively. The anisotropic Von Kármán PSD is then

$$V_\phi(\mathbf{f}; \gamma_0) = r_0^{-\frac{5}{3}} Q_\phi(\mathbf{f}; \gamma_0), \quad (5)$$

where the standard (isotropic) Von Kármán PSD is obtained by taking $\gamma_0 = 1$. Equation (5) shows that the value of r_0 determines the scale of the PSD of the phase screens; it thus determines the variance of the phase screens. We estimate r_0 and γ_0 by fitting Eq. (5) to the spatial PSD of the measured data as described below.

The estimation of r_0 from data requires an estimate of the spatial PSD $\hat{V}_\phi^{\text{meas}}(\mathbf{f})$ of the measured data. For this we use Welch's method,⁵⁹ in which we apply a 2D Hamming window to each image ϕ_n , then find the average over the magnitude-squared FFTs of each image ϕ_n with a 2D Hamming window. We then set the resulting estimate $\hat{V}_\phi^{\text{meas}}(\mathbf{f})$ equal to the right hand side of Eq. (5) (with $L_0 = \hat{L}_0$) and solve for r_0 . Converting from frequency \mathbf{f} to scaled indices $\mathbf{k}\Delta_f$, this yields

$$\hat{r}_0(\mathbf{k}\Delta_f, \gamma_0) = \left(\frac{Q_\phi(\mathbf{k}\Delta_f; \gamma_0)}{\hat{V}_\phi^{\text{meas}}(\mathbf{k}\Delta_f)} \right)^{3/5}. \quad (6)$$

In the isotropic case, $\hat{r}_0(\mathbf{k}\Delta_f, \gamma_0 = 1)$ should be constant, independent of \mathbf{k} , although this is never precisely true for measured data. In the anisotropic case, $\gamma_0 \neq 1$ means that $\hat{r}(\mathbf{k}\Delta_f, \gamma_0)$

varies with \mathbf{k} . Thus, for a fixed γ_0 we take an average over \mathbf{k} to estimate r_0 as a function of γ_0 :

$$\hat{r}_0(\gamma_0) = \text{average}\{\hat{r}(\mathbf{k}\Delta_f, \gamma_0) : \mathbf{k} \in \mathcal{K}\}, \quad (7)$$

where \mathcal{K} is a set of indices $\mathbf{k} = (k_0, k_1)$ that excludes the indices where $k_0 = 0$ or $k_1 = 0$ and excludes the k_{\max} smallest and largest frequency bins along each axis. We exclude the zero indices because the zero frequencies are distorted by TTP removal, and we exclude the edge frequencies because they can be contaminated by aliasing. The frequency cut-off k_{\max} is data-dependent.

Finally, we estimate γ_0 by fitting to the 2D structure function of the measured data, which is defined in Sec. 4. The level sets of the 2D structure function are elliptical, with eccentricity varying with γ_0 . Each value of γ_0 yields an estimate $\hat{r}_0(\gamma_0)$, which together yield a corresponding 2D structure function. Hence, we do a 1D optimization in γ_0 to minimize the mean-squared error between the structure function for this γ_0 and the structure function of the measured data. We take $\hat{\gamma}_0$ to be the value that minimizes this error. If the measured data is assumed to be isotropic, we choose $\hat{\gamma}_0 = 1$.

3.2 Estimating the Flow Velocity

The velocity vector $\mathbf{v} = (v_x, v_y)$ gives the translation (or flow) in pixels from time step $n - 1$ to n as in Eq. (2) (both assumed to be TTP-removed). After T time steps, we obtain a pixel shift of $T\mathbf{v}$, which gives rise to a correlation peak between pixels $\phi_{n-T}(\mathbf{i} - T\mathbf{v})$ and $\phi_n(\mathbf{i})$ where $\mathbf{i} = (i_x, i_y)$ and we use interpolation for fractional pixel shifts. Thus, we can estimate \mathbf{v} by locating correlation peaks between ϕ_n and the T -step flow of ϕ_{n-T} . However, choosing T is difficult because (1) small values of T may not give precise estimates due to numerical ill-conditioning and (2) large values

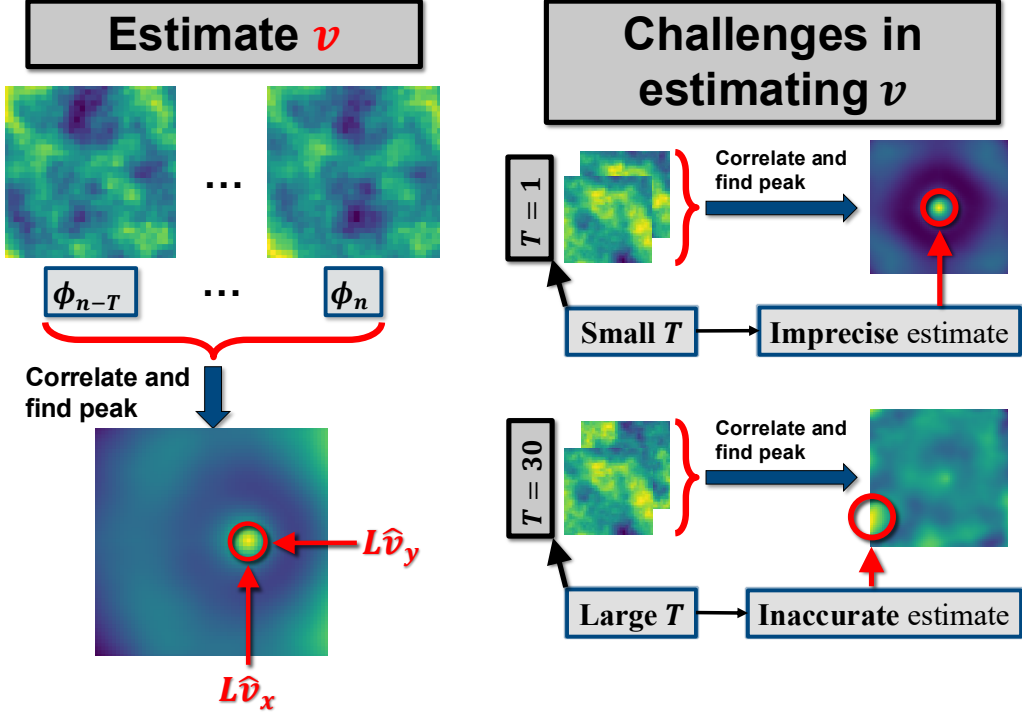


Fig 3: Left: Estimation of the flow velocity \mathbf{v} . Given a time-lag T , we find \mathbf{v} to maximize the correlation between ϕ_n and $\text{Flow}(\phi_{n-T}; T\mathbf{v})$, then average $\mathbf{v}(T)$ over T between 1 and T_{\max} . **Right:** Uncertainty in the time-shift T . Small values of T yield imprecise estimates of the flow velocity due to limited data and numerical ill-conditioning, while large T yield inaccurate estimates due to the decorrelation induced by boiling.

of T will include frames with significant boiling, leading to de-correlation with the earlier frames.

To mitigate this issue, we average the estimates over multiple values of T .

Figure 3, left, illustrates our estimation algorithm for \mathbf{v} . For each time-shift T , we find the cross-correlation between frames at $n - T$ and n as a function of \mathbf{v} as

$$R_{\phi'}(\mathbf{v}; T) = \mathbb{E} \left[\sum_i \phi'_{n-T}(\mathbf{i} - T\mathbf{v}) \phi'_n(\mathbf{i}) \right], \quad (8)$$

where ϕ'_n denotes the mean-subtracted ϕ_n divided by its standard deviation, and we approximate the expected value using an average over n (which we denote $\hat{R}_{\phi'}$). We then take a maximum over

\mathbf{v} to find

$$\hat{\mathbf{v}}(T) = \frac{1}{T} \times \operatorname{argmax}_{\mathbf{v}} \hat{R}_{\phi'}(\mathbf{v}; T). \quad (9)$$

Finally, we average $\hat{\mathbf{v}}(T)$ over $T \in \{1, \dots, T_{\max} - 1\}$, where T_{\max} is chosen based on conditions we describe next.

Figure 3, right, illustrates the considerations in choosing the value of T_{\max} . Small values of T_{\max} may not yield a precise estimate due to limited data and numerical ill-conditioning. Conversely, large values of T_{\max} may give inaccurate estimates because the cross-correlation $R_{\phi'}$ becomes contaminated by boiling. We thus determine T_{\max} based on two criteria. First, note that for sufficiently large values of T depending on the true value of \mathbf{v} , the shift $\mathbf{i} - T\mathbf{v}$ will lie outside the aperture for all \mathbf{i} . In this case, the estimate $\hat{R}_{\phi'}(\mathbf{v}; T)$ will not capture the correlations induced by flow. Thus, we constrain

$$T_{\max} \leq \left\lfloor \frac{N - 1}{\|\hat{\mathbf{v}}\|_{\max}} \right\rfloor, \quad (10)$$

where $\|\hat{\mathbf{v}}\|_{\max}$ is the largest magnitude $\|\hat{\mathbf{v}}(T)\|$ over all time-lags T , and N is the side length in pixels. Additionally, for large T depending on the rate of boiling, the boiling component may obscure the correlations due to flow. To prevent this, we require that the signal-to-noise ratio (SNR) of the estimate $\hat{R}_{\phi'}(\mathbf{v}; T)$ be at least 10 for each T . The resulting bound for T_{\max} is given in Appendix A.

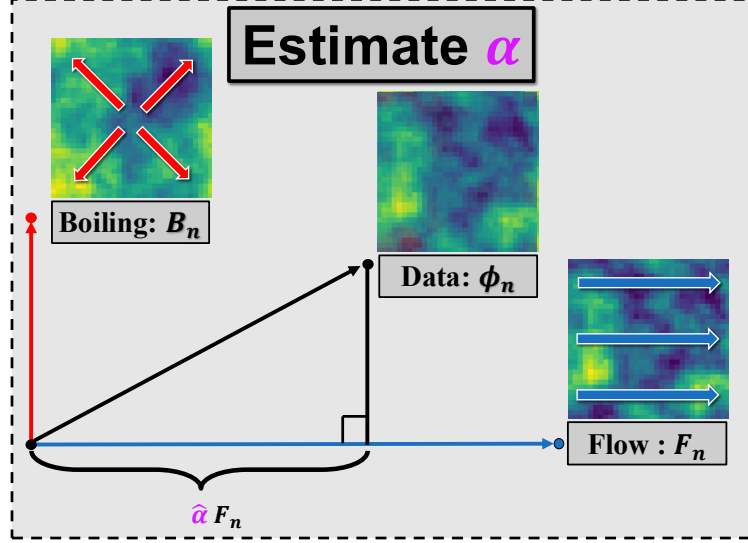


Fig 4: Estimation of the flow-coefficient α . The expected inner product between boiling B_n and flow F_n is 0, so we estimate the flow-coefficient α by projecting the data onto the 1D span of F_n . In practice, we do this projection in Fourier space since F_n is computed in Fourier space, and we make use of all times steps n .

3.3 Estimating the Flow-Coefficient

The flow-coefficient α determines the effect of flow relative to boiling. From Eq. (3), $\phi_n = \sqrt{1 - \alpha^2} B_n + \alpha F_n$ is a linear combination of boiling B_n and the flow F_n of ϕ_{n-1} . Since B_n and ϕ_{n-1} are zero-mean Gaussians which are independent of one another, the expected inner product $\mathbb{E}[\langle B_n, F_n \rangle]$ is 0. Hence we regard B_n and F_n as orthogonal vectors and project ϕ_n onto the span of F_n to estimate α . This estimation of α is equivalent to finding α to minimize the norm of $\phi_n - \alpha F_n$; we use this latter formulation since it is more amenable to incorporating all times step simultaneously. We also do the calculation in Fourier space since the flow is performed natively in Fourier space.

Figure 4 illustrates the geometric intuition for estimating α . In practice, we first estimate v as above, then compute \tilde{F}_n in Eq. (2) using FFTs of the measured data (assumed to be TTP-removed as above). In addition, we remove TTP from \tilde{F}_n and enforce conjugate-symmetry. We then find

the least-squares fit in Fourier space:

$$\hat{\alpha} = \operatorname{argmin}_{\alpha} \left\{ \sum_{n=1}^{N_T-1} \left\| \tilde{\phi}_n - \alpha \tilde{F}_n \right\|^2 \right\}. \quad (11)$$

Here, N_T is the number of time-steps of training data. As with estimating r_0 , we exclude any frequency bins containing a zero frequency and the smallest and largest k_{\max} frequency bins along each axis to reduce the effects of TTP-removal and potential aliasing. Taking the derivative with respect to α allows us to find $\hat{\alpha}$ using only two inner products.

4 Two-Dimensional Structure Function

In this section, we define the two-dimensional phase structure function. Given a separation vector $\mathbf{r} \in \mathbb{R}^2$, the 2D phase structure function is given by

$$D_\phi(\mathbf{r}) = \mathbb{E} \left[(\phi(\mathbf{x} + \mathbf{r}) - \phi(\mathbf{x}))^2 \right], \quad (12)$$

where $\phi(\mathbf{x})$ is the phase error at grid location $\mathbf{x} = (x, y)$, and the expectation is over phase screens ϕ . We make the assumption that ϕ is spatially stationary, so that D_ϕ is not a function of \mathbf{x} . The phase structure function has been widely used to characterize the phase aberrations imposed by atmospheric turbulence.^{25,29,45}

In the case of atmospheric turbulence, the phase structure function depends only on the magnitude of \mathbf{r} . Specifically, because phase errors induced by atmospheric turbulence are spatially

homogeneous and isotropic,^{25,29,45} Eq. (12) follows the Kolmogorov fifth-third power law

$$D_\phi(\mathbf{r}) = 6.88 \left(\frac{\|\mathbf{r}\|}{r_0} \right)^{5/3}, \quad (13)$$

where r_0 is the Fried coherence length. This property is instrumental for generating atmospheric phase screens.²⁹ Furthermore, because Eq. (13) is independent of the angle $\angle \mathbf{r}$, it is inherently a function of the one-dimensional separation distance $\|\mathbf{r}\|$.

However, for anisotropic aero-optic effects, D_ϕ depends on the angle of \mathbf{r} and the magnitude,^{60,61} so Eq. (13) no longer applies. Thus, we compute Eq. (12) as a function of the two-dimensional separation vector \mathbf{r} .

4.1 Estimation from Discrete Data

Although \mathbf{r} is often presented as a continuous input with units of distance, we estimate the structure function from discrete data $\phi_n(\mathbf{i})$, where $\mathbf{i} = (i_x, i_y)$ lies in a discrete set of indices into the 2D array ϕ_n . To avoid interpolation, we restrict \mathbf{r} to vectors of the form $(\mathbf{i}_1 - \mathbf{i}_2)\Delta$, where $\Delta > 0$ is the pixel width in meters.

To estimate the structure function, we first normalize a phase screen as in the estimation of \mathbf{v} to obtain ϕ' . Using the approach of Ref. 25, we compute a quasi-homogeneous structure matrix

$$\hat{D}_{\phi'}^{qh}(\mathbf{i}_1, \mathbf{i}_1) = 2(1 - \mathbb{E}[\phi'(\mathbf{i}_1) \phi'(\mathbf{i}_2)]), \quad (14)$$

where we use time-averages to approximate the expected value. Since the expectation in Eq. (12)

is unchanged after replacing \mathbf{r} with $-\mathbf{r}$, we estimate the 2D phase structure function via

$$\hat{D}_\phi(\mathbf{r}) = \text{average} \left\{ \hat{D}_{\phi'}^{qh}(\mathbf{i}_1, \mathbf{i}_2) : \mathbf{i}_1, \mathbf{i}_2 \text{ satisfy } (\mathbf{i}_1 - \mathbf{i}_2)\Delta = \pm \mathbf{r} \right\}. \quad (15)$$

5 Data and Metrics

In this section, we describe the simulated and measured data along with the metrics used to evaluate our parameter estimation methods.

5.1 Simulated Data

We generate simulated data by choosing boiling flow parameters and then generating data using Eqs. (1), (2), and (3). For each data set, we fix the outer scale L_0 (equal to the aperture length), Fried coherence length r_0 , anisotropy parameter $\gamma_0 = 1$, vertical flow velocity component $v_y = 0$, and temporal sampling rate $f_s = 100$ kHz.

Table 1: Ground-Truth Parameters of Isotropic Simulated Data. Note that each line for v_x corresponds to physical flow velocities 17.2, 34.4, 68.8, 137.5 in meters per second.

Fixed Parameters				
Aperture Width	Fried Param.	Anisotropy Param.	Vertical Vel.	Temp. sampling rate
$L_0 = 44$ mm	$r_0 = 4.4$ mm	$\gamma_0 = 1$	$v_y = 0$	$f_s = 100$ kHz

Variable Parameters		
Image Dimension N (pixels)	Flow Velocity v_x (pixels per time-step)	Flow-Coefficient α (unitless)
20	0.08, 0.16, 0.31, 0.63	
32	0.13, 0.25, 0.5, 1.0	0.1, 0.3, 0.5, 0.7, 0.9
64	0.25, 0.5, 1.0, 2.0	

We investigate the effects of pixel width, flow velocity, and flow-coefficient by varying N , v_x , and α for different data sets. We use physical flow rates of 17.2, 34.4, 68.8, 137.5 meters per second and convert to pixels per time step as follows. With a fixed aperture width of L_0 meters, the pixel

width is given by $\Delta = L_0/N$ in meters per pixel, and so $v_x = (\text{velocity in m/s})/(f_s\Delta)$ in pixels per time step.

Table 1 shows the parameter values used to generate simulated data.

5.2 Measured Data

To evaluate results from measured data, we used two turbulent boundary layer (TBL) data sets containing measured aero-optic phase aberrations obtained from a high-speed wind tunnel experiment.^{7,62} The phase screen data was measured using a Shack Hartmann Wavefront Sensor, with TTP removed from the data.

Table 2 shows details of the resulting aero-optic phase screen data. Note that the image dimensions $M \times N$ are not square. Additionally, a subset of pixels near the boundary had no data. Therefore, we generated boiling flow data with dimension $\max\{M, N\}$ and applied a mask to match the largest inscribed square containing valid data. Since the measured data showed contamination at low temporal frequencies (i.e., sharp peaks at frequencies below 1 kHz, possibly due to vibrations), we pre-processed both measured data sets to remove these additional signals; Appendix B describes this process.

Table 2: Measured Data Sets F06 and F12

	F06	F12
Image Dimension $M \times N$	25×34	21×22
Largest Inscribed Square Length [pixels]	22	18
Pixel Spacing Δ [mm]	1.43	2.24
Sampling Frequency f_s [kHz]	100	130

5.3 Quality Metrics

We evaluate our parameter fitting method using the temporal power spectrum (TPS) and the 2D structure function. We compute the TPS of the phase screens themselves and of the spatial finite difference of the phase screens in the x -direction (i.e., the deflection angle θ_x ^{7,49,63}). For a phase screen ϕ , we call these S_ϕ and S_{θ_x} , respectively. We estimate the TPS of each pixel (in units of energy per second) using the approach of Refs. 31, 64 by applying a Hamming window on multiple subsets of the time samples and then averaging the resulting TPS estimates over all pixels and subsets. We compute the 2D structure function D_ϕ using the approach outlined in Sec. 4.1.

To evaluate the accuracy of parameter estimation for v_x and α , we plot the relative errors $\|\hat{\mathbf{v}} - \mathbf{v}\|/\|\mathbf{v}\|$ and $|\hat{\alpha} - \alpha|/|\alpha|$, and we report the relative error for r_0 .

To measure the statistics of generated data compared to given data, we use normalized root-mean squared error (NRMSE). Here, the normalization is given by dividing by $P_{95}(\mathbf{y}) - P_5(\mathbf{y})$, where $P_m(\mathbf{y})$ denotes the m th percentile of data \mathbf{y} . Specifically, given two arrays $\mathbf{y}, \mathbf{y}^{\text{data}} \in \mathbb{R}^K$, we define

$$\text{NRMSE}(\mathbf{y}, \mathbf{y}^{\text{data}}) = \frac{\frac{1}{\sqrt{K}} \|\mathbf{y} - \mathbf{y}^{\text{data}}\|_2}{P_{95}(\mathbf{y}^{\text{data}}) - P_5(\mathbf{y}^{\text{data}})}, \quad (16)$$

where $\|\cdot\|_2$ is the vector L_2 norm.

We report the following errors, where in each case a superscript “data” indicates values obtained using the simulated or measured data, and a hat indicates values obtained from generated data using estimated parameters.

- **Flow TPS Error:** $\text{NRMSE}(\hat{S}_{\theta_x}, S_{\theta_x}^{\text{data}})$.

- **Phase TPS Error:** $\text{NRMSE}(\hat{S}_\phi, S_\phi^{\text{data}})$.
- **Structure Function Error:** $\text{NRMSE}\left(\sqrt{\hat{D}_\phi}, \sqrt{D_\phi^{\text{data}}}\right)$.

We take the square root of D_ϕ to more evenly weight the large and small values of the structure function.

6 Results

In this section, we show results from the parameter estimation algorithm described in Sec. 3 applied to both isotropic simulated data and anisotropic measured aero-optic data. For all experiments, we used the frequency bin cut-off $k_{\max} = 2$ when estimating r_0 and α . We evaluate our method using the error metrics of the previous section.

6.1 Results from Simulated Data

For each choice of ground-truth parameters, we generated ten independent, $10K$ time-step ‘ground-truth’ boiling flow data sets for parameter estimation and an additional $50K$ time-step data set for error evaluation. For each of these ten generated data sets, we applied our estimation algorithm for isotropic phase screens (i.e., setting $\hat{\gamma}_0 = 1$) and then used the resulting parameter estimates to generate $50K$ -time-step boiling flow data sets. We computed the errors from Sec. 5.3 using this generated $50K$ data set along with the $50K$ evaluation data, then averaged over the ten data sets.

6.1.1 Parameter estimation results

Figure 5, top, plots the relative error $\|\hat{\mathbf{v}} - \mathbf{v}\|/\|\mathbf{v}\|$ of the flow velocity estimates as a function of various ground-truth values of v_x and α . Our velocity estimates are generally more accurate for larger ground-truth values of α (less boiling relative to flow) and larger ground-truth flow velocities

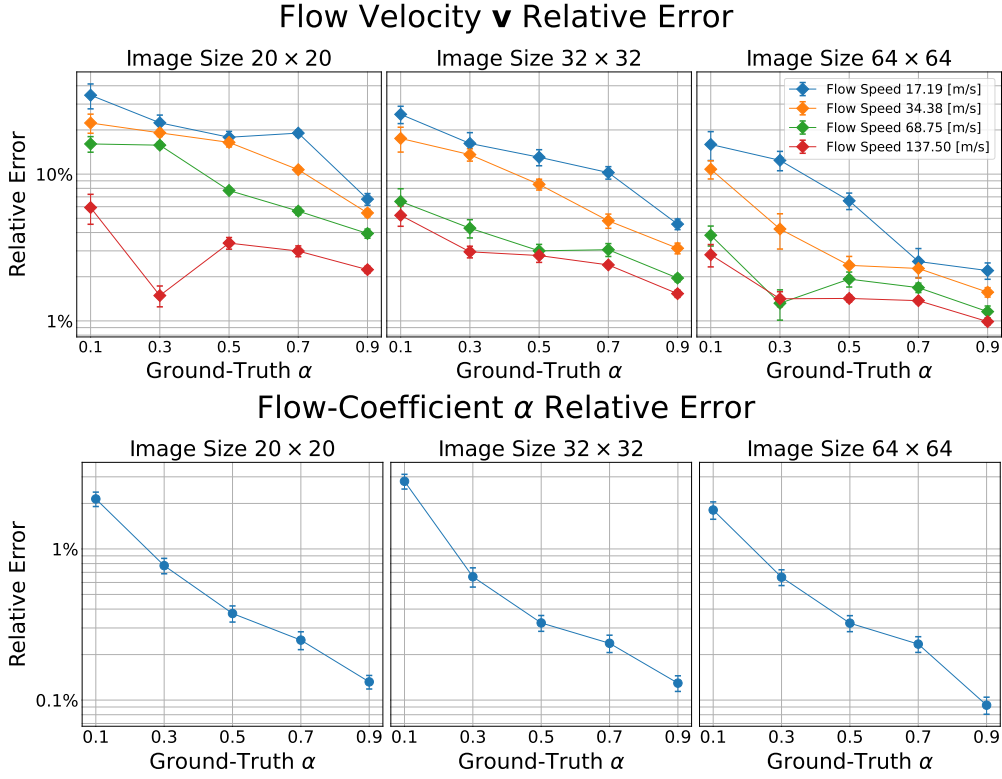


Fig 5: Top: Relative errors of the flow velocity estimates for various image sizes, ground-truth values of α (horizontal axis), and physical velocity (color). Note that the errors are generally smallest for (1) large ground-truth values of α (less boiling relative to flow), (2) large ground-truth flow speeds (larger pixel displacements per time step), and (3) large images. The errors are below 10% in the majority of cases. **Bottom:** Relative errors of the flow-coefficient estimates $\hat{\alpha}$ for various image sizes and ground-truth values of α . Note that the errors are smallest for large ground-truth values of α (less boiling relative to flow) and are slightly lower for larger image sizes. Importantly, the errors remain below 4% in all cases.

(larger pixel displacements per time step); there is also a small improvement in the estimates for larger images. Although the errors can exceed 30% in the edge case that $N = 20$ and the ground-truth α is 0.1, the errors remain below 10% in the majority of cases.

Figure 5, bottom, plots the relative error $|\hat{\alpha} - \alpha|/|\alpha|$ of the flow-coefficient estimates $\hat{\alpha}$ as a function of the ground-truth α . This error showed little dependence on ground-truth flow speeds, so we averaged the errors over all ground-truth v_x . The estimates $\hat{\alpha}$ are significantly more accurate for larger ground-truth values of α . However, there is only a marginal improvement in accuracy for larger images. The errors remain below 1% in most cases and rise to 2-3% only when the

ground-truth α is 0.1.

The accuracy of the estimate \hat{r}_0 depends only on the image size. Different ground truth velocities and flow-coefficients α do not modify the spatial PSD estimate of data with sufficiently many time-steps, so the estimate \hat{r}_0 does not vary significantly across different ground-truth values of v_x and α . The average relative errors of the r_0 estimates were 3.8%, 1.9%, and 1.1% for $N = 20, 32$, and 64, respectively. Thus, the accuracy of the estimates increases significantly with larger image sizes but the errors remain below 4% in all cases.

6.1.2 Simulated data TPS and structure function errors

Figure 6, top, plots the flow TPS error for various ground-truth values of α and physical velocity. Consistent with the estimates of \hat{r}_0 and $\hat{\alpha}$, the flow TPS errors decrease significantly with larger images and larger ground-truth values of α . However, since the flow TPS is sensitive to changes in the flow velocity, small errors in the estimate \hat{v} can cause large flow TPS errors. As a result, even though the relative error in \hat{v} decreases with larger ground truth velocities, the absolute error increases, and so the flow TPS errors also increase with larger flow speeds. Despite this, the errors exceed 10% only when the ground-truth α is 0.1, and they remain below 8% when $\alpha > 0.1$.

Figure 6, bottom, plots the phase TPS errors for various ground-truth values of α . Unlike the flow TPS, the phase TPS has only weak dependence on the flow velocity, so we average over velocity and plot as a function of α alone. As with the errors of the estimates \hat{r}_0 and $\hat{\alpha}$, the phase TPS error decreases for larger images and larger ground-truth values of α . Specifically, the errors exceed 10% only in the edge case that $N = 20$ and the ground-truth α is 0.1.

The structure function NRMSE defined in Sec. 5.3 depends at most weakly on the ground-truth values of α or velocity because the estimate (15) averages over time and boiling flow generates tem-

porally stationary data. Averaging over everything except image size, the average structure function NRMSE values were below 1.2% for each image size, with the error varying only marginally as a function of image size.

6.1.3 Simulated data TPS and structure function examples

Figure 7 shows the TPS and structure function results for simulated data with $N = 64$, ground truth velocity of 137.5 (m/s), and $\alpha = 0.9$. With this choice of parameters, the estimated TPS and structure function both closely match the reference TPS and structure function.

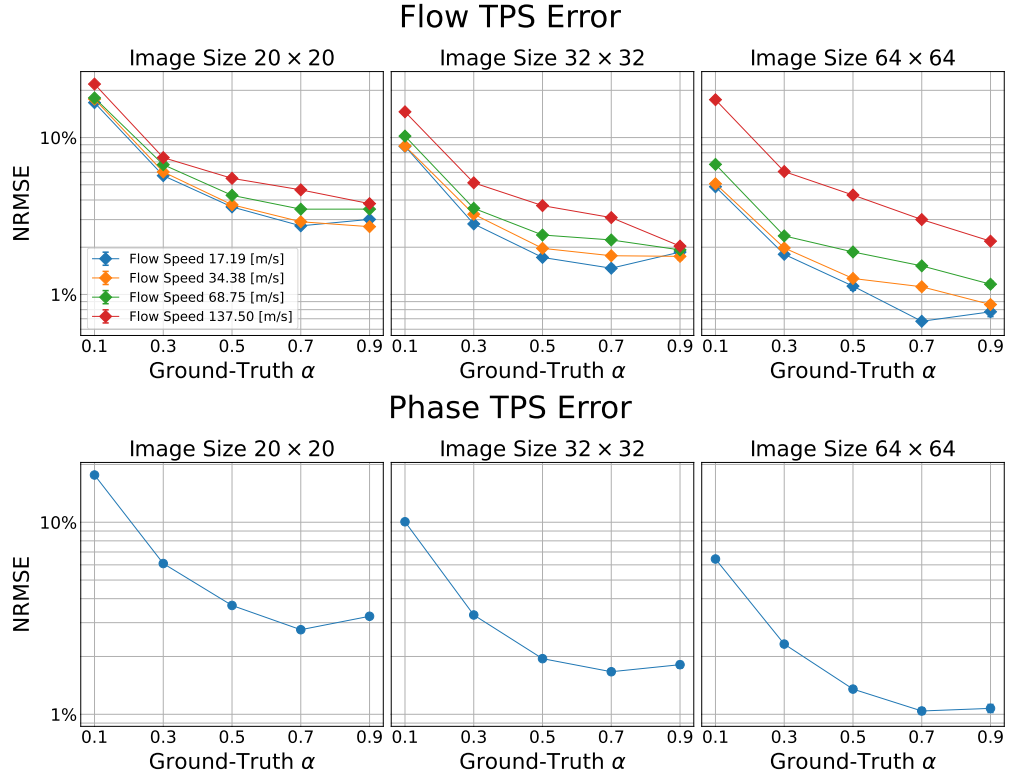


Fig 6: Top: Flow Temporal Power Spectrum (TPS) NRMSE for various image sizes, ground-truth values of α (horizontal axis), and ground truth velocity (color). Note that the errors are smallest for (1) larger images, (2) larger ground-truth values of α , and (3) smaller ground-truth velocities. While the errors can exceed 20% when $\alpha = 0.1$, they remain below 10% when $\alpha > 0.1$. **Bottom:** Phase Temporal Power Spectrum (TPS) NRMSE for various ground-truth values of α . The errors are smallest for larger images and larger ground-truth values of α , and they exceed 10% only in the edge case with 20×20 images and $\alpha = 0.1$.

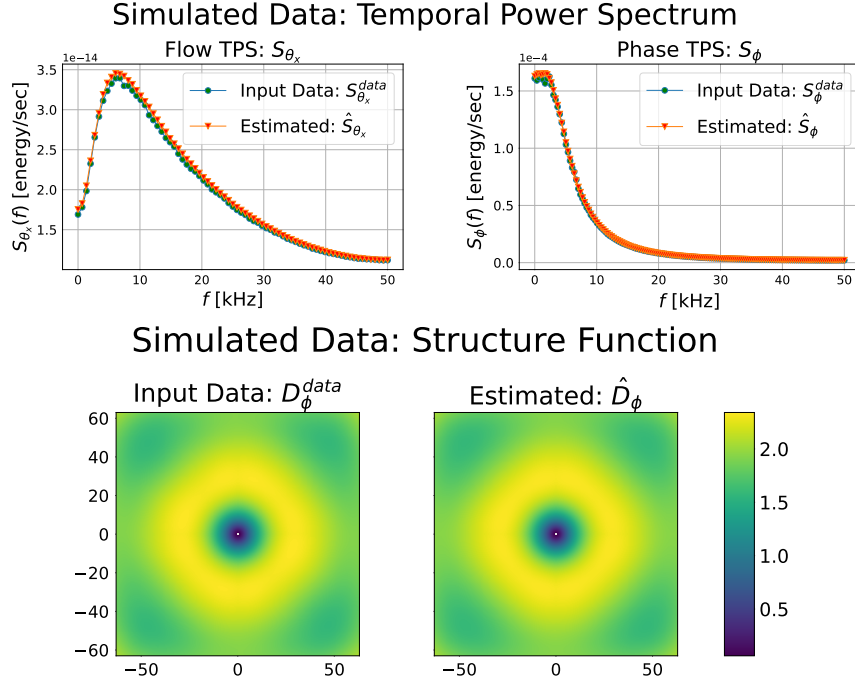


Fig 7: Isotropic estimation from simulated data. **Top:** Comparisons of power spectra obtained from input data (blue) and from isotropic boiling flow data using estimated parameters (orange). The input data has image size 64×64 , flow speed $v_x = 137.5$ (m/s), and $\alpha = 0.9$. The estimated TPS closely matches the reference TPS for both flow, S_{θ_x} , and phase, S_{ϕ} . **Bottom:** Comparison of the structure functions (15) obtained from input data (left) and data using estimated parameters (right). The image size, flow speed, and α are the same as the top figure. The estimated structure function closely matches the reference structure function.

6.2 Results from Measured Data

We applied our parameter estimation algorithm to each data set F06 and F12 from Table 2. We used the first 80% of each measured time series for estimation and used the remaining 20% for error evaluation. For each data set, we estimated boiling flow parameters using both standard isotropic boiling flow ($\hat{\gamma}_0 = 1$) and our newly introduced anisotropic boiling flow ($\hat{\gamma}_0$ estimated from data). We then used these parameter estimates to generate ten isotropic and anisotropic data sets, each with ten times the samples of the evaluation time series. We computed the errors from Sec. 5.3 using these generated data sets versus the 20% error evaluation data, then averaged over the ten data sets.

6.2.1 Isotropic estimation

Table 3 shows the parameter estimates obtained using isotropic boiling flow to fit each measured data set. The large values of $\hat{\alpha}$ indicate that the measured data sets are dominated by flow and have minimal boiling. Further, the flow velocity estimates \hat{v} show that each flow is streamwise along the x -axis and varies by a factor of 2 between data sets F06 and F12.

Table 3: Parameter Estimates from Measured Data - Isotropic Boiling Flow

Parameter Data Set	\hat{L}_0 [mm]	\hat{r}_0 [mm]	\hat{v} [pixels per time-step]	$\hat{\alpha}$
F06	48.62	144.26	(1.20, -0.02)	0.96
F12	49.28	141.78	(0.55, -0.01)	0.95

Figure 8 shows the TPS and structure function results for measured data sets F06 and F12, again using isotropic boiling flow. Here, we plot the flow TPS as a function of frequency f [kHz]; plots of the pre-multiplied flow TPS as a function of Strouhal number can be found in Appendix C. In each case, the estimated flow TPS closely matches the flow TPS of the measured data. Further, the estimated phase TPS closely matches the measured phase TPS at frequencies above 10 kHz. However, the contours of the estimated structure function are circles, while the contours of the measured structure function are ellipses.

Table 4 shows the error metrics for each data set under the isotropic boiling flow approximation. Our parameter estimation algorithm for isotropic phase screens matches the flow and phase TPS of the measured aero-optic data within 5% to 12% NRMSE but has roughly 30% NRMSE for the 2D structure function. Thus, isotropic boiling flow captures the temporal statistics of the data reasonably well both visually and quantitatively, but does not capture the anisotropic spatial correlations of aero-optic phase screen data.

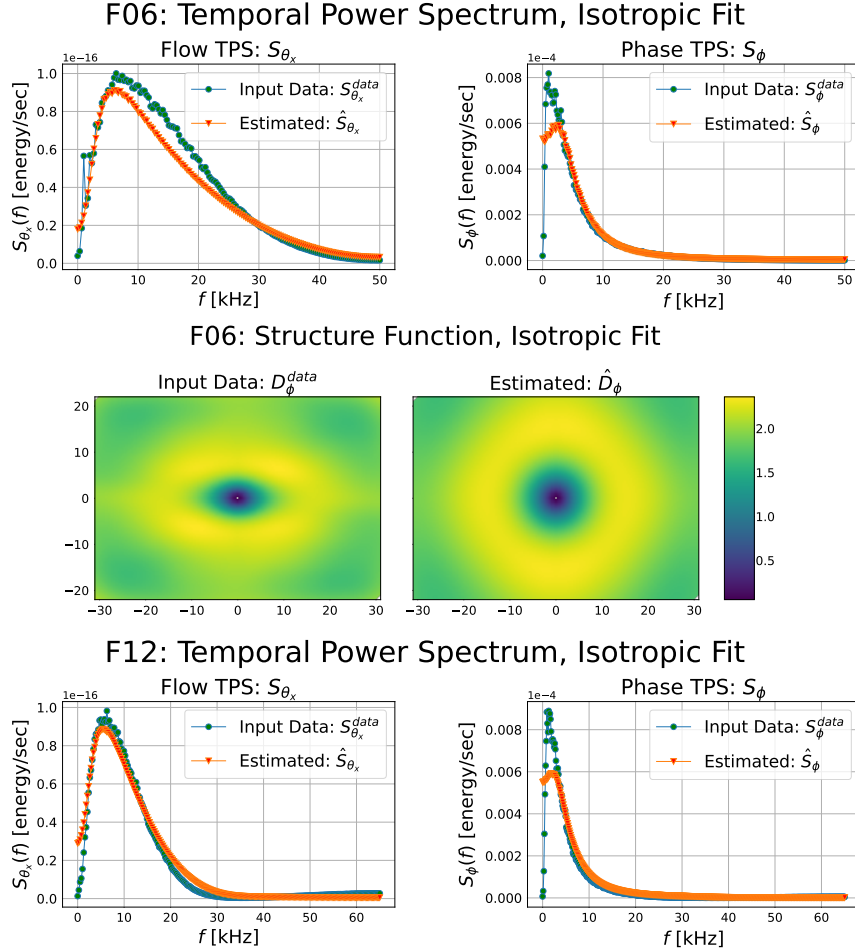


Fig 8: Isotropic estimation from measured data. **Top:** Comparisons of power spectra obtained from measured data set F06 (blue) and from isotropic boiling flow data using estimated parameters (orange). The estimated flow TPS at top left matches the measured TPS reasonably well outside an underestimate in 5-25kHz, while the estimated phase TPS at top right matches at all but the lowest frequencies. **Second row:** Comparison of the 2D structure functions (15) obtained from measured data set F06 (left) and from isotropic boiling flow data using estimated parameters (right). The estimated structure function gives an isotropic fit to the measured structure function but does not match its anisotropic statistics. **Third row:** Results analogous to the top row but for data set F12. Again the TPS fit is good except some mid-range frequencies for the flow TPS and low frequencies for the phase TPS. **Not shown:** The structure function for F12 from estimated isotropic data shows a similar mismatch as for F06.

6.2.2 Anisotropic estimation

Table 5 shows the parameter estimates obtained using anisotropic boiling flow to fit each measured data set. Since the anisotropic and isotropic parameter estimation algorithms differ only in the estimation of r_0 and γ_0 , the estimates of L_0 , v , and α are identical to those in Table 3. The low

Table 4: Error Metrics from Measured Data - Isotropic Boiling Flow

Data Set	NRMSE	F06	F12
Flow TPS	8.36%	5.40%	
Phase TPS	8.78%	11.67%	
Structure Function	32.64%	28.60%	

values of $\hat{\gamma}_0$ indicate that the spatial correlation length scale is much smaller in the y -axis than in the x -axis for both measured data sets. Further, since the algorithm for estimating r_0 depends on the value of $\hat{\gamma}_0$, the resulting \hat{r}_0 values for anisotropic boiling flow vary significantly from the estimates for isotropic boiling flow.

Table 5: Parameter Estimates from Measured Data - Anisotropic Boiling Flow

Data Set	Parameter	\hat{r}_0 [mm]	$\hat{\gamma}_0$	\hat{L}_0	\hat{v}	$\hat{\alpha}$
F06	320.46	0.18				
F12	235.60	0.31	Same as Table 3			

Figures 9 and 10 show the TPS and structure function results for measured data sets F06 and F12, respectively, again using anisotropic boiling flow. As with Fig. 8, we plot the flow TPS as a function of frequency f [kHz]; the pre-multiplied flow TPS as a function of Strouhal number is plotted in Appendix C. In this case, neither the estimated flow TPS nor estimated phase TPS match the measured TPS as closely as isotropic boiling flow. However, the estimated structure functions more closely match the measured structure functions for both data sets, especially at low separation distances. Specifically, the elliptical contours of the estimated structure function more closely match those of the measured structure function. This suggests that anisotropic boiling flow captures the anisotropic spatial correlations of aero-optic phase screen data but do not match the TPS.

Table 6 shows the error metrics for each data set using anisotropic boiling flow. We first note

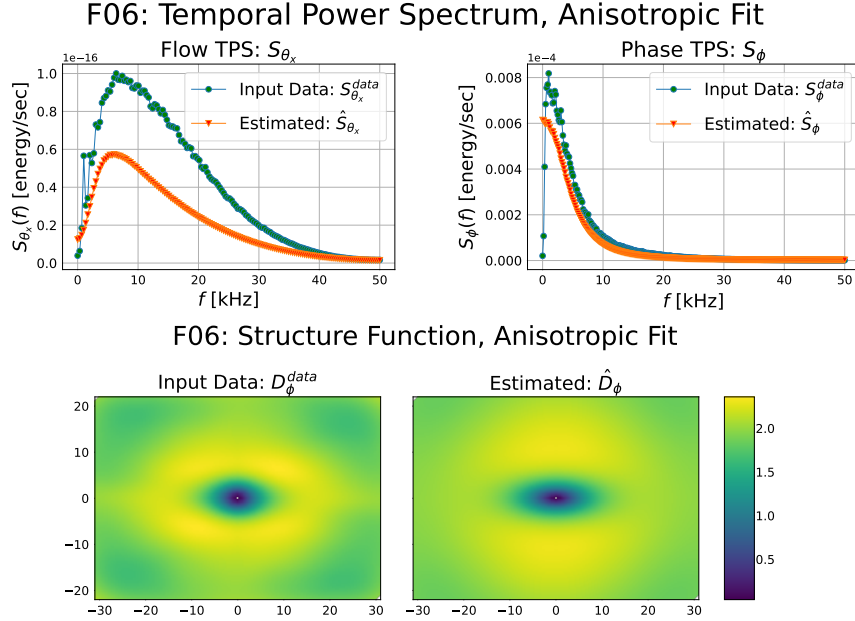


Fig 9: Anisotropic estimation from measured data. **Top:** Comparisons of power spectra obtained from measured data set F06 (blue) and from anisotropic boiling flow data using estimated parameters (orange). The estimated TPS matches the reference TPS for both flow, S_{θ_x} , and phase, S_{ϕ} , at high frequencies but does not match either reference TPS at low and mid-range frequencies. **Bottom:** Comparison of the structure functions (15) obtained from measured data set F06 (left) and from anisotropic boiling flow data using estimated parameters (right). The estimated structure function matches the reference structure function, D_{ϕ} better than the isotropic estimates in Fig. 8

that our parameter estimation algorithm for anisotropic phase screens has 11-27% NRMSE for the flow and phase TPS, significantly larger than isotropic boiling flow. However, it has a structure function NRMSE between 18-26%, much lower than isotropic boiling flow. Thus, while anisotropic boiling flow does not match the temporal statistics of the measured data, it matches the structure function more closely than isotropic boiling flow and better captures the anisotropic spatial correlations of the aero-optic data.

Table 6: Error Metrics from Measured Data - Anisotropic Boiling Flow

NRMSE \ Data Set	F06	F12
Flow TPS	26.10%	12.27%
Phase TPS	11.28%	12.67%
Structure Function	25.25%	18.23%

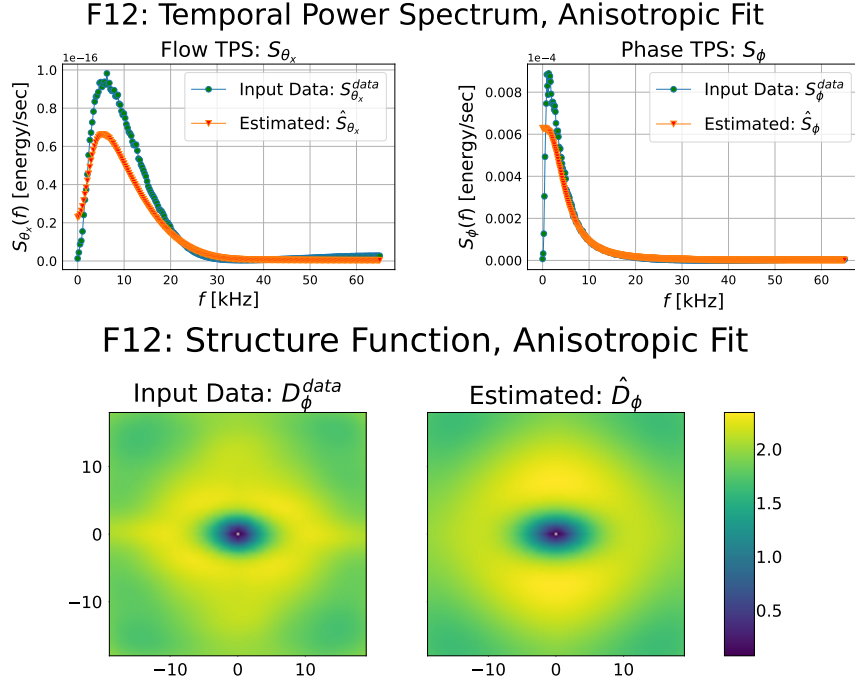


Fig 10: Results analogous to Fig. 9 but for data set F12.

7 Conclusions

In this paper, we introduced a method for applying a well-known atmospheric phase screen generation method, boiling flow, to aero-optic phase screen generation. We (1) introduced an algorithm for estimating the parameters of boiling flow from measured phase screen data and (2) generalized boiling flow to generate spatially anisotropic phase screens. This method can generate arbitrary-duration time series of spatially isotropic or anisotropic aero-optic phase screens using few parameters, offering a less expensive approach than physical experiments or computational fluid dynamics simulations.

We tested this method on both isotropic simulated boiling flow data with known parameter values and anisotropic measured aero-optic data.⁷ The results indicate that our method matches both the temporal power spectrum (TPS) and 2D phase structure function of the isotropic simulated data. Furthermore, while this model does not closely match both the TPS and structure function

of the measured data simultaneously, it can match reasonably well either the TPS using isotropic boiling flow or the structure function using anisotropic boiling flow.

Appendix A: Bound for T_{\max} in the Flow Velocity Estimation Algorithm

In this section, we derive the lower bound for the peak cross-correlation estimate $\hat{R}_{\phi'}(\hat{\mathbf{v}}; T)$ enforced for each time-lag T in the flow velocity estimation algorithm in Sec. 3.2:

$$\hat{R}_{\phi'}(\hat{\mathbf{v}}; T) \geq \frac{15\sqrt{2}}{\sqrt{N_T - T}}. \quad (17)$$

We show that, if this bound holds, then the SNR of the estimate $\hat{R}_{\phi'}(\hat{\mathbf{v}}; T)$ is at least 10, with 5σ confidence. Requiring that this SNR is at least 10 significantly reduces the probability that the flow velocity estimate $\hat{\mathbf{v}}(T)$ is obscured by boiling. Enforcing this bound for each time-lag T is equivalent to setting

$$T_{\max} \leq \max \left\{ T : \hat{R}_{\phi'}(\hat{\mathbf{v}}; T) \geq \frac{15\sqrt{2}}{\sqrt{N_T - T}} \right\} \quad (18)$$

in the flow velocity estimation algorithm.

Note that, for $n \geq T$, Eq. (3) has an image space representation:

$$\phi'_n(\mathbf{i}) = \alpha^T \phi'_{n-T}(\mathbf{i} - T\mathbf{v}^{\text{gt}}) + \sqrt{1 - \alpha^2} \sum_{t=0}^{T-1} \alpha^t B'_{n-t}(\mathbf{i} - t\mathbf{v}^{\text{gt}}). \quad (19)$$

Here, ϕ'_n denotes the the mean-subtracted ϕ_n divided by its standard deviation, B'_n denotes the corresponding (normalized) image-space boiling component (1), and \mathbf{v}^{gt} is the ground-truth flow velocity. Note that, while the components of $\mathbf{i} - t\mathbf{v}^{\text{gt}}$ may not be integers, these positions are

still well-defined given the spatial grid spacing Δ . Given the assumptions of boiling flow and the effect of TTP removal, it follows that both ϕ'_n and B'_n follow a zero-mean, wide-sense stationary multivariate Gaussian distribution (assuming the effect of tip/tilt removal on the distribution of each object is minimal), where each component has unit variance. Furthermore, B'_m is independent of ϕ'_n for all $m > n$.

We compute the SNR for an input \mathbf{v} and time-lag T , which we denote $\text{SNR}(\mathbf{v}, T)$, as the ratio between the mean and standard deviation of the estimate $\hat{R}_{\phi'}(\mathbf{v}; T)$ of Eq. (8). We compute this estimate using an average over the time series and over the pixel pairs in the aperture, so the mean of this estimate $\mu_{\hat{R}}(\mathbf{v}; T)$ is equal to $R_{\phi'}(\mathbf{v}; T)$. We use Eq. (19), the assumed statistical properties of ϕ'_n and B'_n , and an additional assumption that $\phi'_{n-T}(\mathbf{i} - T\mathbf{v})\phi'_n(\mathbf{i})$ and $\phi'_{m-T}(\mathbf{i} - T\mathbf{v})\phi'_m(\mathbf{i})$ are independent for $n \neq m$ to derive an upper bound for the variance of this estimate:

$$\text{Var}[\hat{R}_{\phi'}(\mathbf{v}; T)] \leq \frac{1}{N_T - T} \text{Var}[\phi'_n(\mathbf{i})\phi'_{n-T}(\mathbf{i} - \mathbf{v})] \quad (20)$$

$$= \frac{1}{N_T - T} (1 + R_{\phi'}^2(\mathbf{v}; T)). \quad (21)$$

Here, N_T is the number of time-steps of training data. Importantly, this upper bound applies for all inputs \mathbf{v} .

Defining $\sigma_{\hat{R}}(\mathbf{v}; T) = \sqrt{\text{Var}[\hat{R}_{\phi'}(\mathbf{v}; T)]}$, we may then derive a lower bound for $\text{SNR}(\mathbf{v}, T)$:

$$\text{SNR}(\mathbf{v}, T) = \frac{\mu_{\hat{R}}(\mathbf{v}; T)}{\sigma_{\hat{R}}(\mathbf{v}; T)} \quad (22)$$

$$\geq \sqrt{N_T - T} \times \frac{R_{\phi'}(\mathbf{v}; T)}{\sqrt{1 + R_{\phi'}^2(\mathbf{v}; T)}}. \quad (23)$$

Since $R_{\phi'}(\mathbf{v}; T) \leq 1$ for all \mathbf{v} ,

$$\sigma_{\hat{R}}(\mathbf{v}; T) \leq \frac{\sqrt{2}}{\sqrt{N_T - T}}, \quad (24)$$

$$\text{SNR}(\mathbf{v}, T) \geq \sqrt{N_T - T} \times \frac{R_{\phi'}(\mathbf{v}; T)}{\sqrt{2}}. \quad (25)$$

Thus, if

$$R_{\phi'}(\mathbf{v}; T) \geq \frac{10\sqrt{2}}{\sqrt{N_T - T}}, \quad (26)$$

then the SNR of the estimate $\hat{R}_{\phi'}(\mathbf{v}; T)$ is at least 10.

We wish to enforce $\text{SNR}(\hat{\mathbf{v}}, T) \geq 10$ for each T . That is, we require only that the peak cross-correlation estimate $\hat{R}_{\phi'}(\hat{\mathbf{v}}; T)$ has an SNR of at least 10. To accomplish this, we enforce the bound (26) for $\mathbf{v} = \hat{\mathbf{v}}$ at each T . Since we do not have access to the value of $R_{\phi'}(\mathbf{v}; T)$, we substitute our estimate $\hat{R}_{\phi'}(\hat{\mathbf{v}}; T)$ into the LHS of (26) with 5σ confidence:

$$\hat{R}_{\phi'}(\hat{\mathbf{v}}; T) \pm 5\sigma_{\hat{R}}(\hat{\mathbf{v}}; T) \geq \frac{10\sqrt{2}}{\sqrt{N_T - T}}. \quad (27)$$

Given the bound on the standard deviation (24), we may conclude that if (17) holds, then (26) holds for $\mathbf{v} = \hat{\mathbf{v}}$ with 5σ confidence.

Appendix B: Pre-Processing Measured Data Sets

We applied FIR filters to the measured data sets F06 and F12 before applying our parameter estimation algorithm. We used both notch filters and band-stop filters to remove low-frequency peaks in the TPS of each data set.

The notch filters use a modulated hamming window to reduce the TPS value at a given frequency f_0 [Hz] by a factor $r \in (0, 1)$. To construct a notch filter, we first generate a Hamming window h_n of length N_W and compute

$$g_n = h_n * \cos\left(2\pi \frac{f_0}{f_s} n\right), \quad (28)$$

where f_s [Hz] is the temporal sampling frequency of the data set (listed in Table 2). We then normalize g_n by its frequency response at f_0 :

$$\tilde{g}_n = \frac{g_n}{\sum_{m=0}^{N_W-1} g_m \cos\left(2\pi \frac{f_0}{f_s} m\right)}. \quad (29)$$

Finally, given a ratio $r \in (0, 1)$, we use the impulse response

$$\delta_n - (1 - \sqrt{r})\tilde{g}_n \quad (30)$$

for the notch FIR filter.

Similarly, the band-stop filters use a modulated sinc function to reduce the TPS values in a frequency range $f \in (f_1, f_2)$ [Hz] by a factor of $r \in (0, 1)$. To construct this filter, we first identify the center frequency $f_0 = \frac{1}{2}(f_1 + f_2)$ and frequency range $f_r = \frac{1}{2}(f_2 - f_1)$ and then generate a scaled sinc function

$$g_n = 2f_r \operatorname{sinc}(2\pi f_r n) \quad (31)$$

of length N_W . Next, we apply a Hamming window h_n of the same length to obtain $\tilde{g}_n = h_n g_n$ and

modulate the windowed sinc function via

$$b_n = \tilde{g}_n * \cos \left(2\pi \frac{f_0}{f_s} n \right). \quad (32)$$

As with the notch filter, we then normalize the modulated sinc function via

$$\tilde{b}_n = \frac{b_n}{\sum_{m=0}^{N_W-1} b_m \cos \left(2\pi \frac{f_0}{f_s} m \right)}. \quad (33)$$

Finally, we compute

$$\delta_n - (1 - \sqrt{r})\tilde{b}_n, \quad (34)$$

the impulse response of the band-stop filter.

Tables 7 and 8 list the parameters of each filter applied to F06 and F12, respectively. The filter length N_W determines the bandwidth of the notch filter and the frequency resolution of both filters.

Table 7: Parameters of F06 Pre-Processing Filters

Filter Type	N_W	f_r	f_0	r
Band-Stop	2001	350	850	0.81
Notch	1029	N/A	683.59	0.81
Notch	2049	N/A	976.56	0.81

Table 8: Parameters of F12 Pre-Processing Filters

Filter Type	N_W	f_r	f_0	r
Band-Stop	2001	300	1000	0.81
Notch	2049	N/A	900	0.95

Appendix C: Pre-Multiplied Flow TPS Plots as a Function of Strouhal Number

In this section, we show the pre-multiplied flow TPS as a function of the Strouhal number St_δ for both measured data sets. The Strouhal number is a unit-less quantity given by

$$St_\delta = \frac{f \times \delta^*}{U_c}, \quad (35)$$

where f is the temporal frequency in Hz, δ^* is the boundary layer thickness in meters, and U_c is the convective velocity in meters per second. For both measured data sets F06 and F12, we used $\delta^* = 15.6$ mm, as estimated in Refs. 7, 62. We computed $U_c = \hat{v}_x \Delta f_s$ using the flow velocity estimates \hat{v}_x from Table 3 and pixel spacing Δ and sampling frequency f_s from Table 2; this resulted in values $U_c = 172.37$ for F06 and $U_c = 160.26$ for F12.

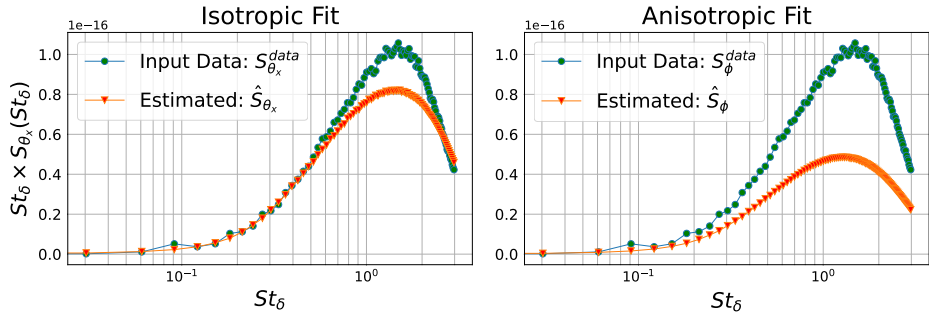
Figure 11 shows the pre-multiplied flow TPS results as a function of the Strouhal number St_δ for both measured data sets F06 and F12. We include results for both isotropic and anisotropic boiling flow. The y -axis of each plot shows the flow TPS multiplied by the Strouhal number input, $St_\delta \times S_{\theta_x}(St_\delta)$. Further, in these plots, we include pre-multiplied flow TPS values up to $St_\delta = 3$ for F06 and up to $St_\delta = 2$ for F12; we exclude the highest frequencies since the measured data sets appeared to be aliased. These results illustrate a similar fit to the flow TPS as the results in Figs. 8, 9, and 10.

Disclosures

The views expressed are those of the author and do not necessarily reflect the official policy or position of the Department of the Air Force, the Department of Defense, or the U.S. Government. Approved for public release; distribution is unlimited. Public Affairs release approval # 2025-5580.

Approved for public release; distribution is unlimited. Public Affairs release approval # 2025-5580.

F06: Pre-Multiplied Flow TPS: $St_\delta \times S_{\theta_x}(St_\delta)$



F12: Pre-Multiplied Flow TPS: $St_\delta \times S_{\theta_x}(St_\delta)$

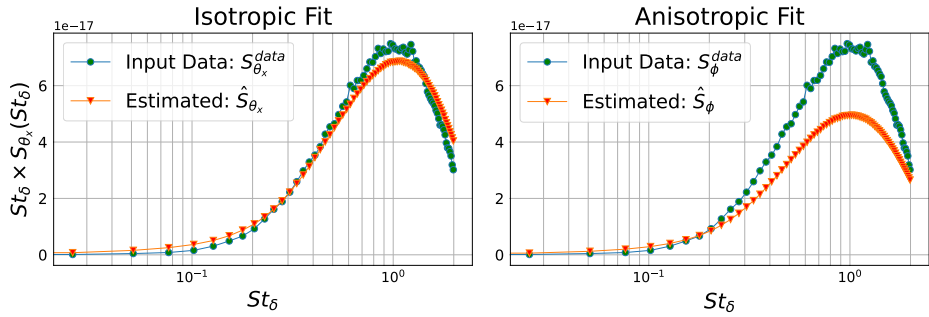


Fig 11: Comparisons of the pre-multiplied flow temporal power spectrum (TPS) as a function of Strouhal number St_δ obtained from measured data (blue) and from boiling flow data using estimated parameters (orange). **Top:** data set F06. **Bottom:** data set F12. Results include both isotropic boiling flow (left) and anisotropic boiling flow (right).

Code, Data, and Materials Availability

The code used to generate the results and figures is available in a Github repository linked in Ref. 47.

The measured data sets used in this article were taken at the University of Notre Dame in the trisonic wind tunnel facility within the hessert laboratory for aerospace research. For more details concerning the experiment, please refer to Ref. 7. This data is publicly available at the following link: <https://www.datadepot.rcac.purdue.edu/bouman/>.

Acknowledgments

C.A.B. was partially supported by the Showalter Trust. J.W.U., G.T.B., and C.A.B. were partially supported by AFRL/RDKL FA9451-20-2-0008. The authors would like to thank the Showalter family and the United States Air Force for supporting this research.

References

- 1 V. I. Tatarski, *Wave Propagation in a Turbulent Medium*, ch. 4, 59–80. Dover, Mineola, New York (1961). English translation of the original Russian edition.
- 2 M. Wang, A. Mani, and S. Gordeyev, “Physics and computation of aero-optics,” *Annual Review of Fluid Mechanics* **44**(1), 299–321 (2012). [doi:10.1146/annurev-fluid-120710-101152].
- 3 E. J. Fitzgerald and E. J. Jumper, “The optical distortion mechanism in a nearly incompressible free shear layer,” *Journal of fluid mechanics* **512**, 153–189 (2004). [doi:10.1017/S0022112004009553].
- 4 M. R. Visbal and D. P. Rizzetta, “Effect of flow excitation on aero-optical aberration,” in *46th AIAA Aerospace Sciences Meeting and Exhibit*, 1074, American Institute of Aeronautics and Astronautics (2008). [doi:10.2514/6.2008-1074].
- 5 L. A. Chernov, *Wave Propagation in a Random Medium*, ch. 5, 58–83. McGraw-Hill Book Company, Inc., Mineola, New York (1960). English translation of the original Russian edition.
- 6 M. Kalensky, S. Gordeyev, M. R. Kemnetz, *et al.*, “Aero-optical effects, part i. system-level considerations: tutorial,” *J. Opt. Soc. Am. A* **41**, 2163–2174 (2024). [doi:10.1364/JOSAA.533763].

- 7 M. R. Kemnetz and S. Gordeyev, “Optical investigation of large-scale boundary-layer structures,” in *54th AIAA Aerospace Sciences Meeting*, 1460, American Institute of Aeronautics and Astronautics (2016). [doi:10.2514/6.2016-1460].
- 8 J. M. Geary, *Introduction to wavefront sensors*, vol. TT18 of *Tutorial texts in optical engineering*, ch. 5-7, 53–103. SPIE Optical Engineering Press, Bellingham, Washington (1995).
- 9 R. B. Holmes, “Adaptive optics for directed energy: Fundamentals and methodology,” *AIAA journal* **60**(10), 5633–5644 (2022). [doi:10.2514/1.J061766].
- 10 B. D. Shaffer, A. J. McDaniel, C. C. Wilcox, *et al.*, “Dynamic mode decomposition based predictive model performance on supersonic and transonic aero-optical wavefront measurements,” *Appl. Opt.* **60**, G170–G180 (2021). [doi:10.1364/AO.426031].
- 11 J. N. Kutz, D. Sashidhar, S. Sahba, *et al.*, “Physics-informed machine-learning for modeling aero-optics,” in *Applied Optical Metrology IV*, E. Novak, J. D. Trolinger, and C. C. Wilcox, Eds., *Proc. SPIE* **11817**, 118170E (2021). [doi:10.1117/12.2596540].
- 12 B. D. Shaffer, A. J. McDaniel, and C. C. Wilcox, “Predictive modeling of wavefront error using dynamic mode decomposition,” in *Interferometry XX*, M. B. N. Morris, K. Creath, and R. Porras-Aguilar, Eds., *Proc. SPIE* **11490**, 114900E (2020). [doi:10.1117/12.2569869].
- 13 S. Sahba, D. Sashidhar, C. C. Wilcox, *et al.*, “Dynamic mode decomposition for aero-optic wavefront characterization,” *Optical Engineering* **61**(1), 013105 (2022). [doi:10.1117/1.OE.61.1.013105].
- 14 B. D. Shaffer, J. R. Vorenberg, C. C. Wilcox, *et al.*, “Neural network forecasting of transonic turbulent flow for adaptive optics control,” in *Unconventional Imaging and Adaptive*

- Optics 2022*, J. J. Dolne and M. F. Spencer, Eds., *Proc. SPIE* **12239**, 122390H (2022). [doi:10.1117/12.2631995].
- 15 R. Burns, E. Jumper, and S. Gordeyev, “A latency-tolerant architecture for airborne adaptive optic systems,” in *53rd AIAA Aerospace Sciences Meeting*, 0679, American Institute of Aeronautics and Astronautics (2015). [doi:10.2514/6.2015-0679].
- 16 R. Burns, E. Jumper, and S. Gordeyev, “A robust modification of a predictive adaptive-optic control method for aero-optics,” in *47th AIAA Plasmadynamics and Lasers Conference*, 3529, American Institute of Aeronautics and Astronautics (2016). [doi:10.2514/6.2016-3529].
- 17 R. Burns, S. Gordeyev, E. Jumper, *et al.*, “Estimation of aero-optical wavefronts using optical and non-optical measurements,” in *52nd AIAA Aerospace Sciences Meeting*, 0319, American Institute of Aeronautics and Astronautics (2014). [doi:10.2514/6.2014-0319].
- 18 E. J. Jumper, M. A. Zenk, S. V. Gordeyev, *et al.*, “Airborne Aero-Optics Laboratory,” *Optical Engineering* **52**(7), 071408 (2013). [doi:10.1117/1.OE.52.7.071408].
- 19 E. J. Jumper and S. Gordeyev, “Physics and measurement of aero-optical effects: Past and present,” *Annual Review of Fluid Mechanics* **49**(1), 419–441 (2017). [doi:10.1146/annurev-fluid-010816-060315].
- 20 K. Wang and M. Wang, “Aero-optics of subsonic turbulent boundary layers,” *Journal of Fluid Mechanics* **696**, 122–151 (2012). [doi:10.1017/jfm.2012.11].
- 21 K. Wang, M. Wang, S. Gordeyev, *et al.*, “Computation of aero-optical distortions over a cylindrical turret with passive flow control,” in *41st Plasmadynamics and Lasers Conference*, 4498, American Institute of Aeronautics and Astronautics (2010). [doi:10.2514/6.2010-4498].

- 22 C. Porter, M. Rennie, and E. Jumper, “Computation of the aero-optical environment of a helicopter using prescribed-wake methods,” *AIAA journal* **53**(3), 532–541 (2015). [doi:10.2514/1.J052969].
- 23 S. Gordeyev and E. Jumper, “Fluid dynamics and aero-optical environment around turrets,” in *40th AIAA Plasmadynamics and Lasers Conference*, 4224, American Institute of Aeronautics and Astronautics (2009). [doi:10.2514/6.2009-4224].
- 24 S. Gordeyev and E. Jumper, “Fluid dynamics and aero-optics of turrets,” *Progress in Aerospace Sciences* **46**(8), 388–400 (2010). [doi:10.1016/j.paerosci.2010.06.001].
- 25 C. R. Vogel, G. A. Tyler, and D. J. Wittich, “Spatial-temporal-covariance-based modeling, analysis, and simulation of aero-optics wavefront aberrations,” *J. Opt. Soc. Am. A* **31**, 1666–1679 (2014). [doi:10.1364/JOSAA.31.001666].
- 26 J. W. Utley, G. T. Buzzard, C. A. Bouman, *et al.*, “Data-driven synthetic wavefront generation for boundary layer data,” in *Unconventional Imaging, Sensing, and Adaptive Optics 2024*, J. J. Dolne, S. R. Bose-Pillai, and M. Kalensky, Eds., *Proc. SPIE* **13149**, 131490A (2024). [doi:10.1117/12.3027740].
- 27 A. Faghihi, J. Tesch, and S. Gibson, “Identified state-space prediction model for aero-optical wavefronts,” *Optical Engineering* **52**(7), 071419 (2013). [doi:10.1117/1.OE.52.7.071419].
- 28 S. Srinath, L. A. Poyneer, A. R. Rudy, *et al.*, “Computationally efficient autoregressive method for generating phase screens with frozen flow and turbulence in optical simulations,” *Opt. Express* **23**, 33335–33349 (2015). [doi:10.1364/OE.23.033335].
- 29 J. D. Schmidt, *Numerical Simulation of Optical Wave Propagation with Examples in MATLAB*, vol. PM199, ch. 9, 149–184. SPIE, United States (2010). [doi:10.1117/3.866274.ch9].

- 30 G. I. Taylor, “The spectrum of turbulence,” *Proceedings of the Royal Society of London. Series A-Mathematical and Physical Sciences* **164**(919), 476–490 (1938). [doi:10.1098/rspa.1938.0032].
- 31 L. Poyneer, M. van Dam, and J.-P. Véran, “Experimental verification of the frozen flow atmospheric turbulence assumption with use of astronomical adaptive optics telemetry,” *J. Opt. Soc. Am. A* **26**, 833–846 (2009). [doi:10.1364/JOSAA.26.000833].
- 32 B. L. Gerard, C. Marois, and R. Galicher, “Fast coherent differential imaging on ground-based telescopes using the self-coherent camera,” *The Astronomical Journal* **156**, 106 (2018). [doi:10.3847/1538-3881/aad23e].
- 33 D. C. Dayton and M. F. Spencer, “Scaled-laboratory demonstrations of deep-turbulence conditions,” *Appl. Opt.* **63**, E54–E63 (2024). [doi:10.1364/AO.520208].
- 34 J. Lin, N. Jovanovic, and M. P. Fitzgerald, “Design considerations of photonic lanterns for diffraction-limited spectrometry,” *J. Opt. Soc. Am. B* **38**, A51–A63 (2021). [doi:10.1364/JOSAB.423664].
- 35 L. A. Poyneer, S. M. Ammons, M. K. Kim, *et al.*, “Laboratory demonstration of the prediction of wind-blown turbulence by adaptive optics at 8 khz with use of lqg control,” *Appl. Opt.* **62**, 1871–1885 (2023). [doi:10.1364/AO.474730].
- 36 P. Jia, W. Wang, R. Ning, *et al.*, “Digital twin of atmospheric turbulence phase screens based on deep neural networks,” *Opt. Express* **30**, 21362–21376 (2022). [doi:10.1364/OE.460244].
- 37 R. Boddeda, D. R. Arrieta, S. Almonacil, *et al.*, “Achievable capacity of geostationary-ground optical links,” *Journal of Lightwave Technology* **41**(12), 3717–3725 (2023). [doi:10.1109/JLT.2023.3271824].

- 38 A. G. Sheikh, C. J. Pellizzari, S. J. Kisner, *et al.*, “Dynamic dh-mbir for phase-error estimation from streaming digital-holography data,” in *2023 57th Asilomar Conference on Signals, Systems, and Computers*, 784–788, IEEE (2023). [doi:10.1109/IEEECONF59524.2023.10477047].
- 39 A. Snyder, S. Srinath, B. Macintosh, *et al.*, “Temporal characterization of Zernike decomposition of atmospheric turbulence,” in *Ground-based and Airborne Telescopes VI*, H. J. Hall, R. Gilmozzi, and H. K. Marshall, Eds., *Proc. SPIE* **9906**, 990642 (2016). [doi:10.1117/12.2234362].
- 40 V. Sridhar, S. J. Kisner, S. P. Midkiff, *et al.*, “Fast algorithms for model-based imaging through turbulence,” in *Artificial Intelligence and Machine Learning in Defense Applications II*, J. Dijk, Ed., *Proc. SPIE* **11543**, 1154304 (2020). [doi:10.1117/12.2570789].
- 41 J. Lehtonen, C. M. Correia, and T. Helin, “Limits of turbulence and outer scale profiling with non-Kolmogorov statistics,” in *Adaptive Optics Systems VI*, L. M. Close, L. Schreiber, and D. Schmidt, Eds., *Proc. SPIE* **10703**, 107036C (2018). [doi:10.1117/12.2313960].
- 42 A. de Pinho e Braga, D. W. Oesch, D. C. Dayton, *et al.*, “Coherence length measurements under strong scintillation conditions using a five-layer laboratory-scaled atmospheric simulator,” in *Conference on Lasers and Electro-Optics, Conference on Lasers and Electro-Optics*, SW4E.7, Optica Publishing Group (2020). [doi:10.1364/CLEO_SI.2020.SW4E.7].
- 43 R. L. Lloyd, T. J. Hardy, M. F. Spencer, *et al.*, “Dynamic image correction and wavefront sensing with a digital holographic sensor using 4D implicit neural representations,” in *Unconventional Imaging, Sensing, and Adaptive Optics 2025*, J. J. Dolne, S. R. Bose-Pillai, and M. Kalensky, Eds., *Proc. SPIE* **13619**, 136190Y (2025). [doi:10.1117/12.3063178].

- 44 A. G. Sheikh, C. J. Pellizzari, S. J. Kisner, *et al.*, “Dynamic DH-MBIR for low-latency wave-front estimation in the presence of atmospheric boiling,” in *Unconventional Imaging, Sensing, and Adaptive Optics 2023*, J. J. Dolne, M. F. Spencer, and S. R. Bose-Pillai, Eds., *Proc. SPIE* **12693**, 1269308 (2023). [doi:10.1117/12.2676406].
- 45 J. P. Siegenthaler, E. J. Jumper, and S. Gordeyev, “Atmospheric propagation vs. aero-optics,” in *46th AIAA Aerospace Sciences Meeting and Exhibit*, 1076, American Institute of Aeronautics and Astronautics (2008). [doi:10.2514/6.2008-1076].
- 46 J. W. Utley, G. T. Buzzard, C. A. Bouman, *et al.*, “Boiling flow parameter estimation from boundary layer data,” in *Unconventional Imaging, Sensing, and Adaptive Optics 2025*, J. J. Dolne, S. R. Bose-Pillai, and M. Kalensky, Eds., *Proc. SPIE* **13619**, 136190L (2025). [doi:10.1117/12.3063655].
- 47 J. W. Utley, G. T. Buzzard, C. A. Bouman, *et al.*, “Boiling flow.” Software library available from https://github.com/jeffreyutley/boiling_flow (2025).
- 48 M. R. Kemnetz and S. Gordeyev, “Analysis of aero-optical jitter in convective turbulent flows using stitching method,” *AIAA Journal* **60**(1), 14–30 (2022). [doi:10.2514/1.J060756].
- 49 J. P. Siegenthaler, S. Gordeyev, and E. Jumper, “Shear layers and aperture effects for aero-optics,” in *36th AIAA Plasmadynamics and Lasers Conference*, 4772, American Institute of Aeronautics and Astronautics (2005). [doi:10.2514/6.2005-4772].
- 50 C. E. Coulman, J. Vernin, Y. Coqueugniot, *et al.*, “Outer scale of turbulence appropriate to modeling refractive-index structure profiles,” *Appl. Opt.* **27**, 155–160 (1988). [doi:10.1364/AO.27.000155].
- 51 D. L. Fried, “Optical resolution through a randomly inhomogeneous medium for

- very long and very short exposures," *J. Opt. Soc. Am.* **56**, 1372–1379 (1966). [doi:10.1364/JOSA.56.001372].
- 52 R. K. Tyson, *Introduction to Adaptive Optics*, ch. 4, 33–44. SPIE, Bellingham, Washington (2000). [doi:10.1117/3.358220].
- 53 R. Avila, A. Ziad, J. Borgnino, *et al.*, "Theoretical spatiotemporal analysis of angle of arrival induced by atmospheric turbulence as observed with the grating scale monitor experiment," *J. Opt. Soc. Am. A* **14**, 3070–3082 (1997). [doi:10.1364/JOSAA.14.003070].
- 54 A. Ziad, R. Conan, A. Tokovinin, *et al.*, "From the grating scale monitor to the generalized seeing monitor," *Appl. Opt.* **39**, 5415–5425 (2000). [doi:10.1364/AO.39.005415].
- 55 A. Ziad, M. Schöck, G. A. Chanan, *et al.*, "Comparison of measurements of the outer scale of turbulence by three different techniques," *Appl. Opt.* **43**, 2316–2324 (2004). [doi:10.1364/AO.43.002316].
- 56 F. Martin, A. Tokovinin, A. Agabi, *et al.*, "Gsm: a grating scale monitor for atmospheric turbulence measurements. i. the instrument and first results of angle of arrival measurements," *Astronomy and Astrophysics Suppl. Ser.* **108**, 173–180 (1994).
- 57 M. Schöck, D. L. Mignant, G. A. Chanan, *et al.*, "Atmospheric turbulence characterization with the keck adaptive optics systems. i. open-loop data," *Appl. Opt.* **42**, 3705–3720 (2003). [doi:10.1364/AO.42.003705].
- 58 P. P. Andrade, P. J. Garcia, C. M. Correia, *et al.*, "Estimation of atmospheric turbulence parameters from shack–hartmann wavefront sensor measurements," *Monthly Notices of the Royal Astronomical Society* **483**, 1192–1201 (2018). [doi:10.1093/mnras/sty3181].
- 59 P. Welch, "The use of fast fourier transform for the estimation of power spectra: A method

- based on time averaging over short, modified periodograms,” *IEEE Transactions on Audio and Electroacoustics* **15**(2), 70–73 (1967). [doi:10.1109/TAU.1967.1161901].
- 60 S. Rasouli, E. Mohammadi Razi, and J. Niemela, “Investigation of the anisotropy and scaling of the phase structure function of a spatially coherent light beam propagating through convective air turbulence,” *J. Opt. Soc. Am. A* **39**, 1641–1649 (2022). [doi:10.1364/JOSAA.464285].
- 61 E. E. Silbaugh, B. M. Welsh, and M. C. Roggemann, “Characterization of atmospheric turbulence phase statistics using wave-front slope measurements,” *J. Opt. Soc. Am. A* **13**, 2453–2460 (1996). [doi:10.1364/JOSAA.13.002453].
- 62 M. Kemnetz, *Analysis of the Aero-Optical Component of the Jitter Using the Stitching Method*. PhD thesis, University of Notre Dame (2019). [doi:10.7274/k930bv76j74].
- 63 J. Cress, S. Gordeyev, M. Post, *et al.*, “Aero-optical measurements in a turbulent, subsonic boundary layer at different elevation angles,” in *39th Plasmadynamics and Lasers Conference*, 4214, American Institute of Aeronautics and Astronautics (2005). [doi:10.2514/6.2008-4214].
- 64 A. V. Oppenheim, R. W. Schafer, and J. R. Buck, *Discrete-time signal processing*, ch. 9–10, 629–774. Prentice Hall signal processing series, Prentice Hall, Upper Saddle River, NJ, 2nd ed. (1999).

Jeffrey Utley is a PhD candidate in mathematics at Purdue University. He received his BS degree in mathematics from the University of Tennessee in 2022. His current research focuses on generating synthetic aero-optic phase screens using statistical models.

Biographies and photographs of the other authors are not available.

List of Figures

- 1 Outline of the boiling flow algorithm as used in this paper. Starting with a time series of measured phase screens ϕ_n , our method estimates the boiling flow parameters and decomposes the data into the weighted sum of a boiling component and a flow component. The method then uses these components and the parameters to generate synthetic phase screens using boiling flow. We introduce the parameter γ_0 into the boiling model to produce spatially anisotropic correlations.
- 2 **Left:** Estimation of the boiling parameters (L_0, r_0) . We set \hat{L}_0 to the aperture length in meters. We then do per-frequency scaling by $(r_0(\mathbf{f}))^{-5/3}$ of the unit-scale Von Kárman PSD to match the spatial PSD of the measured data. Then we average over frequencies to obtain \hat{r}_0 . **Right:** Instead of regarding r_0 as a length scale, we interpret it as a scaling parameter for the spatial PSD of phase screens. Smaller r_0 corresponds to larger variance of the phase screens.
- 3 **Left:** Estimation of the flow velocity \mathbf{v} . Given a time-lag T , we find \mathbf{v} to maximize the correlation between ϕ_n and $\text{Flow}(\phi_{n-T}; T\mathbf{v})$, then average $\mathbf{v}(T)$ over T between 1 and T_{\max} . **Right:** Uncertainty in the time-shift T . Small values of T yield imprecise estimates of the flow velocity due to limited data and numerical ill-conditioning, while large T yield inaccurate estimates due to the decorrelation induced by boiling.

- 4 Estimation of the flow-coefficient α . The expected inner product between boiling B_n and flow F_n is 0, so we estimate the flow-coefficient α by projecting the data onto the 1D span of F_n . In practice, we do this projection in Fourier space since F_n is computed in Fourier space, and we make use of all times steps n .
- 5 **Top:** Relative errors of the flow velocity estimates for various image sizes, ground-truth values of α (horizontal axis), and physical velocity (color). Note that the errors are generally smallest for (1) large ground-truth values of α (less boiling relative to flow), (2) large ground-truth flow speeds (larger pixel displacements per time step), and (3) large images. The errors are below 10% in the majority of cases.
Bottom: Relative errors of the flow-coefficient estimates $\hat{\alpha}$ for various image sizes and ground-truth values of α . Note that the errors are smallest for large ground-truth values of α (less boiling relative to flow) and are slightly lower for larger image sizes. Importantly, the errors remain below 4% in all cases.
- 6 **Top:** Flow Temporal Power Spectrum (TPS) NRMSE for various image sizes, ground-truth values of α (horizontal axis), and ground truth velocity (color). Note that the errors are smallest for (1) larger images, (2) larger ground-truth values of α , and (3) smaller ground-truth velocities. While the errors can exceed 20% when $\alpha = 0.1$, they remain below 10% when $\alpha > 0.1$. **Bottom:** Phase Temporal Power Spectrum (TPS) NRMSE for various ground-truth values of α . The errors are smallest for larger images and larger ground-truth values of α , and they exceed 10% only in the edge case with 20×20 images and $\alpha = 0.1$.

- 7 Isotropic estimation from simulated data. **Top:** Comparisons of power spectra obtained from input data (blue) and from isotropic boiling flow data using estimated parameters (orange). The input data has image size 64×64 , flow speed $v_x = 137.5$ (m/s), and $\alpha = 0.9$. The estimated TPS closely matches the reference TPS for both flow, S_{θ_x} , and phase, S_ϕ . **Bottom:** Comparison of the structure functions (15) obtained from input data (left) and data using estimated parameters (right). The image size, flow speed, and α are the same as the top figure. The estimated structure function closely matches the reference structure function.
- 8 Isotropic estimation from measured data. **Top:** Comparisons of power spectra obtained from measured data set F06 (blue) and from isotropic boiling flow data using estimated parameters (orange). The estimated flow TPS at top left matches the measured TPS reasonably well outside an underestimate in 5-25kHz, while the estimated phase TPS at top right matches at all but the lowest frequencies. **Second row:** Comparison of the 2D structure functions (15) obtained from measured data set F06 (left) and from isotropic boiling flow data using estimated parameters (right). The estimated structure function gives an isotropic fit to the measured structure function but does not match its anisotropic statistics. **Third row:** Results analogous to the top row but for data set F12. Again the TPS fit is good except some mid-range frequencies for the flow TPS and low frequencies for the phase TPS. **Not shown:** The structure function for F12 from estimated isotropic data shows a similar mismatch as for F06.

- 9 Anisotropic estimation from measured data. **Top:** Comparisons of power spectra obtained from measured data set F06 (blue) and from anisotropic boiling flow data using estimated parameters (orange). The estimated TPS matches the reference TPS for both flow, S_{θ_x} , and phase, S_ϕ , at high frequencies but does not match either reference TPS at low and mid-range frequencies. **Bottom:** Comparison of the structure functions (15) obtained from measured data set F06 (left) and from anisotropic boiling flow data using estimated parameters (right). The estimated structure function matches the reference structure function, D_ϕ better than the isotropic estimates in Fig. 8
- 10 Results analogous to Fig. 9 but for data set F12.
- 11 Comparisons of the pre-multiplied flow temporal power spectrum (TPS) as a function of Strouhal number St_δ obtained from measured data (blue) and from boiling flow data using estimated parameters (orange). **Top:** data set F06. **Bottom:** data set F12. Results include both isotropic boiling flow (left) and anisotropic boiling flow (right).

List of Tables

- 1 Ground-Truth Parameters of Isotropic Simulated Data. Note that each line for v_x corresponds to physical flow velocities 17.2, 34.4, 68.8, 137.5 in meters per second.
- 2 Measured Data Sets F06 and F12
- 3 Parameter Estimates from Measured Data - Isotropic Boiling Flow
- 4 Error Metrics from Measured Data - Isotropic Boiling Flow
- 5 Parameter Estimates from Measured Data - Anisotropic Boiling Flow

6 Error Metrics from Measured Data - Anisotropic Boiling Flow

7 Parameters of F06 Pre-Processing Filters

8 Parameters of F12 Pre-Processing Filters